An effective stress analysis for predicting the evolution of SCR-seabed stiffness accounting for consolidation

Manuscript submitted to Géotechnique

Z. Zhou, C. D. O'Loughlin and D. J. White

Zefeng ZHOU (corresponding author)
Centre for Offshore Foundation Systems and ARC Research Hub for Offshore Floating Facilities
University of Western Australia
Perth, WA 6009, Australia
Tel: +61 403848151
Email: zefeng.zhou@research.uwa.edu.au

Conleth D. O'LOUGHLIN
Centre for Offshore Foundation Systems and ARC Research Hub for Offshore Floating Facilities
University of Western Australia
Perth, WA 6009, Australia
Tel: +61 8 6488 7326
Email: conleth.oloughlin@uwa.edu.au

David J. WHITE
University of Southampton
Southampton, Southampton SO17 1BJ, UK
Tel: +44 23 8059 6859
Email: david.white@soton.ac.uk

Number of words (excluding the abstract, list of notation, acknowledgements, references, tables and figure captions): 6954
Number of tables (excluding appendix): 4
Number of figures (excluding appendix): 16

An effective stress analysis for predicting the evolution of SCR-seabed stiffness, accounting for consolidation

Z. ZHOU[1], C. D. O'LOUGHLIN [1] AND D. J. WHITE[2]

Steel catenary risers (SCRs) are an efficient solution to transfer hydrocarbons from deep-water seabeds to floating facilities. SCR design requires an assessment of the fatigue life in the touchdown zone, where the riser interacts with the seabed, which relies on reliable estimates of the SCR-seabed stiffness over the design life.

Current models for SCR-seabed stiffness consider only undrained conditions, neglecting the development and dissipation of excess pore pressures that occur over the life of the SCR. This consolidation process alters the seabed strength and consequently the SCR-seabed stiffness. This paper summarises experimental data that shows that long-term cyclic vertical motion of an SCR at the touchdown zone leads to a reduction in seabed strength due to remoulding and water entrainment, but that this degradation is eclipsed by the regain in soil strength during consolidation.

The main focus of this paper is on prediction of the temporal changes in seabed strength and stiffness due to long-term cyclic shearing and consolidation, to support calculations of SCR-seabed interaction. The predictions are obtained using a framework that considers the change in effective stress and hence soil strength using critical state concepts, and that considers the soil domain as a one-dimensional column of elements. The merit of the model is assessed via simulations of SCR centrifuge model tests with over 3,000 cycles of repeated undrained vertical cycles in normally consolidated kaolin clay. Comparisons of the simulated and measured

[1] *Centre for Offshore Foundation Systems, The University of Western Australia, Crawley, WA 6009, Australia (Corresponding author: Fax +61 403848151; Email: zefeng.zhou@research.uwa.edu.au)*
[2] *University of Southampton, Southampton SO17 1BJ, UK*

profiles of SCR penetration resistance reveal that the model can capture accurately the observed changes in SCR-seabed stiffness. Example simulations show the merit of the model as a tool to assess the timescale in field conditions over which this order of magnitude change in seabed stiffness occurs. It is concluded that current design practice may underestimate the seabed stiffness significantly, but the new approach allows rapid checking of this for particular combinations of SCR and soil conditions.

Keywords: clay, SCR, SCR-seabed interaction, soil strength, SCR penetration resistance, seabed stiffness, consolidation, cyclic loading.

1. INTRODUCTION

Steel catenary risers (SCRs) are an efficient option in deep water for oil and gas transmission from the seabed to a floating structure (see Figure 1a). SCRs undergo long-term cyclic motion due to operational loads from the floating structure and environmental loads from waves and currents. For an element of SCR at the touchdown zone (TDZ), the cyclic shearing of the surrounding soil results in progressive generation of positive excess pore pressure in soft clays. This excess pore pressure causes degradation of the soil strength, and also reductions in stiffness. After reconsolidation periods, dissipation of this excess pore pressure leads to increases in soil strength and stiffness (Hodder et al. 2009; Yuan et al. 2017; Hou et al. 2018).

Assessing the fatigue life of an SCR is one of the most challenging issues in design practice. Fatigue life calculations are strongly influenced by the seabed strength and stiffness at the TDZ (Kimiaei et al. 2010; Li & Low 2012; Queau et al. 2013; Elosta et al. 2013; Elosta et al. 2014). Therefore, an accurate prediction of seabed strength and stiffness is necessary for a reliable assessment of fatigue life.

The majority of the current prediction methods (see summary in Table 1) consider only undrained soil behaviour using a total stress approach, and can include different load-displacement paths at either penetration, uplift, loss-of-contact, or re-penetration (see Figure 1b). The various models differ in how they formulate the hysteretic load-displacement behaviour for the different modes, simplified as either a 'closed hysteresis loop' (e.g. Aubeny & Biscontin, 2009; Voie et al. 2014), or by adopting an 'open hysteresis loop' during SCR penetration and extraction (e.g. You et al. 2008; Randolph & Quiggin 2009; Zargar 2017). In general, the models account for soil strength degradation due to the cyclic motion of the SCR through the formulation adopted for the load-displacement response; for example, by predicting a progressive increase in embedment from cycles of compressive load. However, they do not explicitly link soil strength to the change in effective stress associated with excess pore pressure generation due to undrained shearing.

Recent experimental studies (Hodder et al. 2009; Yuan et al. 2017; Hou et al. 2018) showed that the continued vertical cyclic motion of an SCR at the TDZ in soft clay results in progressive generation of excess pore pressure and degradation of soil strength, with a reduction in stiffness. However, over time dissipation of this excess pore pressure leads to a reduction in specific volume and a regain in soil strength and stiffness. The implication for SCR design is that the choice of soil stiffness in the fatigue analysis should be higher than that associated with full

degradation of the soil strength. Although absolute magnitudes will be controlled by the time scales of interest and the rate at which consolidation progresses, recent experimental evidence (Yuan et al. 2017) shows that over thousands of continuous load cycles the strength and stiffness can recover and surpass the initial values, due to consolidation.

These effects are potentially important in design, as noted in a recent review of the state-of-knowledge of SCR behaviour at the TDZ (Clukey et al. 2017): (1) variations in seabed resistance and stiffness due to consolidation may have a significant influence on the fatigue life; (2) reduction in the uncertainty in fatigue assessments is vital, since many in-service SCRs are reaching the limit of their initial design life.

This paper summarises recent SCR seabed stiffness measurements and compares them with results from effective stress analyses of vertical SCR-seabed interaction at the TDZ. The analyses are based on an effective-stress framework outlined in Zhou et al. (2018) that accounts for changing soil strength due to changes in excess pore water pressure. As applied to an SCR at the TDZ, the main features of the new analysis that extends existing models (as outlined in Table 1) are:

1) The changing seabed strength is captured by calculating the variation in excess pore pressure generated during undrained shearing.

2) The framework is defined with sufficient generality that it can be applied to scenarios that are load-controlled, displacement-controlled or a mixed sequence, such that it allows realistic simulation of 'whole life' cyclic loading histories of SCRs undergoing vertical movement in the TDZ.

3) A nonlinear load-displacement model is used to calculate the mobilisation of the strength and limiting resistance, therefore giving the variation in stiffness. The load-displacement relationship uses a changing tangent stiffness that can predict SCR-seabed interaction during initial penetration, extraction and repenetration.

4) An additional reduction in soil strength due to the effect of water entrainment can be added into the analysis by migrating the fully remoulded strength line (RSL) to reflect higher degradation in soil strength.

After introducing the framework, including application to an SCR in the TDZ, the paper assesses its merit in describing long term SCR-seabed stiffness changes at the TDZ through retrospective simulation of SCR centrifuge tests in normally consolidated kaolin clay reported

in Yuan et al. (2017).

2. DETAILS OF MODEL ANALYSIS

2.1 Introducing the effective stress framework

The analysis considers vertical SCR-seabed interaction so the soil is idealised as a one-dimensional column - in an extension of the widely used oedometer method for foundation settlement. The one-dimensional soil domain is discretised, and the vertical effective stress and soil strength is calculated at each soil horizon throughout the loading sequence. Notation for this study is presented in Figure 1.

The framework is described within the context of an SCR undergoing a history of cyclic vertical motion at the TDZ as shown in Figure 2. To facilitate the calculation, the SCR motion is idealised as episodic, with cycles of a penetration and extraction event (Figure 2a) followed by a 'no-motion' event, while excess pore water pressure dissipates (Figure 2b).

Undrained cyclic motion leads to remoulding of the seabed, with an associated reduction in seabed strength. This loss in strength is recognized as a reduction in effective stress following excess pore water pressure generation. With accumulation of excess pore pressure, u_e, the vertical effective stress, σ'_v, moves towards the fully remoulded strength line (denoted RSL) at constant specific volume for a fully undrained condition. This is represented by the path A-B on Figure 2a, where point B represents a fully remoulded state. During the subsequent consolidation period, dissipation of excess pore pressure will result in an increase in effective stress, σ'_v, and reduction in specific volume, v, represented in Figure 2b by the path B-C' for partial consolidation and the path B-C for full consolidation.

Repenetration of the SCR (Figure 2c) will cause regeneration of excess pore pressure that will reduce σ'_v to a higher limiting value (point D on the RSL, see Figure 2c) than during the initial penetration due to the reduction in v associated with the previous consolidation phase. The increase in $\sigma'_{v,RSL}$ and reduction in v (point B relative to point D on Figure 2c) results in an increase in soil strength, s_u. As the number of episodes of penetration, reconsolidation and repenetration increases (case I in Figure 2d), the magnitude of u_e reduces with progressively diminishing increases in $\sigma'_{v,RSL}$, and hence regain in s_u. Hence, the limiting state is when there are no further changes in pore pressure, such that the undrained shear strength is equal to the equivalent drained value.

In reality the SCR at the TDZ may be subjected to continuous rather than episodic cyclic loading. This is handled by the framework by running the shearing and consolidation steps in sequence with the associated changes in vertical effective stress being very small for every penetration-extraction event. This is represented in Figure 2d (case II) by the effective stress path A-B′-C′ for long-term continuous cyclic undrained shearing, which like the path A-B-C for episodic cyclic undrained shearing, eventually approaches the limiting state.

2.2 Formulating the framework

The analytical components of the effective stress framework are briefly outlined in the following sub-sections, with more details of the framework provided in Zhou et al. (2019).

2.2.1 Excess pore pressure generation

Shear induced excess pore pressure, $u_e(\hat{z})$ ($\hat{z} = z/D$, where z is soil depth and D is SCR diameter), generated by undrained penetration is linked to an (absolute) cumulative shear strain, $\varepsilon(\hat{z})$, at each soil horizon (Zhou et al. 2018). In the present approach, the rate of excess pore pressure generation is close to zero as the vertical effective stress approaches the RSL. The rate of excess pore pressure generation can be expressed as:

$$\frac{\delta u_e(\hat{z})}{\delta \varepsilon(\hat{z})} = \frac{\chi}{\varepsilon_{99}}\left[\frac{u_{e,r}(\hat{z})}{u_{e,max}(\hat{z})}\right]^p = \frac{\chi}{\varepsilon_{99}}\left[\frac{\sigma'_v(\hat{z}) - \sigma'_{v,RSL}(\hat{z})}{\sigma'_{v,NCL}(\hat{z}) - \sigma'_{v,RSL}(\hat{z})}\right]^p \quad (1)$$

where ε_{99} is the characteristic shear strain associated with a degree of remoulding equal to 99% (meaning a 99% reduction in strength from initial to fully remoulded, for an overconsolidation ratio, OCR = 1); p is a constant power that affects the shape of the pore pressure generation and χ is a characteristic pressure that varies with specific volume, v; $u_{e,r}$ is the remaining excess pore pressure defined as the distance between the current effective stress, σ'_v, and the effective stress on the RSL, $\sigma'_{v,RSL}$, (shown in Figure 3); $u_{e,max}$ is the maximum potential excess pore pressure, $u_{e,max} = \sigma'_{v,NCL} - \sigma'_{v,RSL}$ (where $\sigma'_{v,NCL}$ is the vertical effective stress on the normal compression line, NCL). The vertical effective stress on the RSL, $\sigma'_{v,RSL}$, can be expressed directly in terms of the initial specific volume as

$$\sigma'_{v,RSL}(\hat{z}) = \left(\frac{s_u}{\sigma'_{v0}}\right)_{NC} \frac{\sigma'_{v0}(\hat{z})}{\Phi S_t} \exp\left\{\frac{\Lambda\left[\Gamma_{NCL} - v_{initial}(\hat{z}) - \lambda \ln\left(\sigma'_{v0}(\hat{z})\right)\right]}{\lambda - \kappa}\right\} \quad (2)$$

where $(s_u/\sigma'_{vo})_{NC}$ is the normally consolidated undrained strength ratio; Λ is the plastic volumetric strain ratio; Γ_{NCL} is the specific volume at σ'_v = 1 kPa on the NCL; $v_{initial}$ is the initial

specific volume; κ is the gradient of the unloading-reloading line (URL); λ is the gradient of the NCL; S_t is the soil sensitivity and Φ is a lumped strength parameter (described later).

The model is defined such that the changing seabed strength during cycles of penetration and extraction varies in the manner seen in cyclic penetrometer tests (e.g. Hodder et al. 2009). During penetration or extraction, a full passage of a soil element entirely into and out of the zone results in a cumulative (absolute) shear strain increase of Δε = 400% (Einav & Randolph 2005).

2.2.2 Consolidation process

The initial magnitude of excess pore pressure generated by an undrained penetration event thereafter is denoted as $u_{e,i}(\hat{z})$, which is defined at the beginning of every pause period. Dissipation of excess pore pressure during consolidation is described by a simple hyperbolic model (Chatterjee et al. 2013; Zhou et al. 2018), which can be expressed in rate form as

$$\frac{\delta u_e(\hat{z})}{\delta t} = -\frac{u_{e,i}(\hat{z}, t)\, c_v^m t^{m-1} \left(D^2 T_{50}\right)^m m}{\left(\left(D^2 T_{50}\right)^m + \left(c_v t\right)^m\right)^2} \quad (3)$$

where t is the period of (consolidation) time between the penetration and extraction of an SCR at any given depth, c_v is the coefficient of vertical consolidation, m is a constant that controls the shape of the dissipation response and T_{50} is the dimensionless time factor for 50% dissipation of the initial excess pore pressure.

As noted earlier, excess pore pressure dissipation results in a reduction in specific volume and a rise in vertical effective stress towards the equilibrium effective stress, $\sigma'_{eqm}(\hat{z})$ as shown in Figure 2b. The associated change in specific volume, $\triangle v(\hat{z})$, can be obtained from the change in vertical effective stress, $\Delta\sigma'_v(\hat{z})$ (equal to the dissipated excess pore pressure), expressed as:

$$\Delta v(\hat{z}) = -\kappa \ln\left[\frac{\sigma'_v(\hat{z}) + \Delta\sigma'_v(\hat{z})}{\sigma'_v(\hat{z})}\right] \quad (4)$$

2.2.3 Soil strength response

The undrained shear strength, $s_u(\hat{z})$, at each soil horizon is simply calculated from the vertical effective stress via a lumped strength parameter, Φ, given by

$$s_u(\hat{z}) = \Phi\sigma'_v(\hat{z}) \quad (5)$$

where $\sigma'_{\mathrm{v}}(\hat{z}) = \sigma'_{\mathrm{v,eqm}}(\hat{z}) - u_{\mathrm{e}}(\hat{z})$. The lumped strength parameter could be assigned a peak value that decays to a steady value with cumulative shear strain to capture effects from cementation or bonding, over-consolidation, destructuration, and changes in K_0 through shearing events (White & Hodder 2010; Hodder et al. 2013; Zhou et al. 2018).

The shear strength that governs soil resistance is obtained from a strength influence function, $v_{\mathrm{s}}(\hat{z})$. This zone is defined by a triangular function extending by a distance, α, above and below the centreline of the SCR. The averaged undrained shear strength, $s_{\mathrm{u,av}}$, at the current embedment of the SCR, $\hat{z}_{\mathrm{e}}$ is:

$$s_{\mathrm{u,av}} = \int_{\hat{z}_{\mathrm{e}} - \alpha}^{\hat{z}_{\mathrm{e}} + \alpha} s_{\mathrm{u}}\left(\hat{z}\right) v_{\mathrm{s}}\left(\hat{z}\right) \mathrm{d}z \tag{6}$$

2.2.4 Changing seabed stiffness and mobilisation of soil strength

The mobilisation of seabed strength is linked to average undrained shear strength, $s_{\mathrm{u,av}}$, and is captured by a non-linear model, similar to the form used for *p-y* or *t-z* curves for pile-soil interaction. The non-linear model uses a changing tangent stiffness related to the mobilised soil strength, $s_{\mathrm{u,mob}}$. Stiffness will be high as motion begins in a new direction, and ensures the soil strength asymptotically approaches the (spatially-averaged) available soil strength. The incremental change in normalised soil strength during mobilisation, $\delta\left(\frac{s_{\mathrm{u,mob}}}{s_{\mathrm{u,av}}}\right)$, is expressed as

$$\delta\left(\frac{s_{\mathrm{u,mob}}}{s_{\mathrm{u,av}}}\right) = \delta\left(\hat{z}\right) K \tag{7}$$

in which the effective tangent stiffness, *K*, is gradually reduced according to the proportion of the change in mobilised strength that has occurred (including any unloading and reloading). After any reversal, the potential normalised change is defined as $\left(\frac{|\Delta s_{\mathrm{u,max}}|}{s_{\mathrm{u,av}}}\right)$ and lies in the range 0 to 2, and the current normalised change is given by $\left(\frac{|\Delta s_{\mathrm{u,mob}}|}{s_{\mathrm{u,av}}}\right)$ and lies in the range -1 (fully mobilised soil strength during extraction) to 1 (fully mobilised soil strength during penetration), as shown in Figure 4. The effective tangent stiffness is expressed as

$$K = \left(1 - \left(\frac{\Delta\left(\frac{s_{u,mob}}{s_{u,av}}\right)}{\Delta\left(\frac{s_{u,max}}{s_{u,av}}\right)}\right)^{\zeta}\right) K_{max} \quad (8)$$

where ζ is the power law parameter to account for the rate of change in tangent stiffness and is generally in the range 0.1 to 0.5 and K_{max} is the maximum tangent stiffness that is adopted since the last reversal in penetration or extraction. Noting that load cycles may be fully or partially mobilised (see Figure 4a), the selection of K_{max} can be assigned on the basis of variation in $\left(\frac{|\Delta s_{u,max}|}{s_{u,av}}\right)$ (e.g. as shown by the simply linear dependence on Figure 4b). The generality of the framework allows for progressive motion in one-way and two-way cyclic loading with changing soil tangent stiffness (see Figure 4).

2.3 Application of the framework to an element of SCR at the TDZ

Application to an element of SCR interacting with the seabed requires that a depth profile of excess pore pressure is generated for each time step, allowing for a depth profile for effective stress, from which the soil strength and hence the SCR penetration resistance, q, is calculated. The calculation procedure is presented in Figure 5 and described below.

The depth zone over which excess pore pressure is generated due to the passage of the SCR element within the seabed is considered in terms of the incremental shear strain at each soil horizon, $\delta\varepsilon(\hat{z})$. This is quantified by an strain influence function, $\mu(\hat{z})$, when the soil element is close to the SCR within the strain influence zone (see Figure 5b), and expressed as

$$\delta\varepsilon(\hat{z}) = 4\mu(\hat{z})\delta\hat{z}_m \quad (9)$$

where $\delta\hat{z}_m$ is the incremental embedment of the SCR. The strain influence zone is considered as a triangle shape with limits that extend a normalised distance, β, above and below the SCR centerline. If the soil horizon is outside the influence zone, then $\mu(\hat{z}) = 0$, and the soil horizon is unaffected by the current SCR displacement. Integration of the strain rate over the influence zone results in a shear total strain, $\Delta\varepsilon = 400\%$ (based on Einav & Randolph (2005)). Using Equation 1, the vertical spatial distribution of excess pore pressure at each soil horizon, $u_e(\hat{z})$, is calculated and shown in Figure 5c. Vertical effective stress, $\sigma'_v(\hat{z})$, is then calculated in response to any change in excess pore pressure (Figure 5d), allowing for depth profiles of

average soil strength and mobilised soil strength (Figure 5e).

The penetration resistance on the SCR element, q, is the sum of seabed resistance, q_s (Figure 5g), and soil buoyancy, q_b (Figure 5h):

$$q(\hat{z}) = q_s(\hat{z}) + q_b(\hat{z}) \tag{10}$$

in which

$$q_s(\hat{z}) = N_c s_u \tag{11}$$

and

$$q_b(\hat{z}) = f_b A_s \gamma' \frac{1}{D} \tag{12}$$

s_u in Equation 11 is the undrained shear strength predicted by the framework and N_c is a bearing capacity factor (Figure 5f) that varies with depth as the failure mechanism transitions from shallow to deep. This depth variation is allowed for here through (Aubeny & Biscontin 2009; White et al. 2010; Randolph & White 2008a; Merifield et al. 2009)

$$N_c = a\left(\hat{z}\right)^b \tag{13}$$

where a and b are constants taken as a = 7.1 and b = 0.33 for $\hat{z} \leq 0.75$ (rough surface, Merifield et al. 2009), and a = 6 and b = 0.15 for $\hat{z} > 0.75$ (rough surface, Randolph & White 2008a). The pipe surface roughness will change the bearing capacity factor, Nc. In this study, Nc was selected considering a rough surface.

The soil buoyancy term, q_b, in Equation 12 is calculated as the product of the effective unit weight of soil, γ', and the (normal) cross-section area of the embedded segment of the SCR, A_s (Merifield et al. 2009; Hodder et al. 2009). An additional effect of soil heave is captured by a factor, f_b, and it is assumed that f_b decreases linearly from 1.3 (for soft clay) to unity at a critical depth where the failure mechanism is localised to the SCR (White et al. 2010).

3. Effective-stress analysis of SCR-seabed interaction

The SCR element tests reported by Yuan et al. (2017) are summarised here, and simulated using the effective stress model. These tests serve as the best means of assessing the merit of the method as they involve up to 3,000 cycles of SCR penetration and extraction, over a period of time that is sufficient to observe both the reduction and subsequent increase in soil strength and

consequently SCR-seabed vertical stiffness. The tests were conducted in normally consolidated kaolin clay in a geotechnical centrifuge at 50*g*. The SCR was modelled using a segment of pipe with a diameter of 20 mm (1 m at prototype scale) and a length of 120 mm (6 m at prototype scale).

Two tests are considered here, time histories for which are shown in Figure 6. The first was a 'short-term' test, in which the SCR was penetrated from a normalised depth of $\hat{z}$ = -1 (i.e. from one diameter above the mudline) to $\hat{z}$ = 3 for 200 cycles. The second was a 'long-term' test in which the SCR was penetrated from a normalised depth of $\hat{z}$ = -1 to a depth equivalent to an applied pressure, q_p = 8 kPa for 3,000 cycles. In each test the model SCR was penetrated and extracted at a velocity of 2.5 mm/s (at model scale), which was considered sufficient to generate undrained conditions for the two tests. Further details of the tests are provided in Yuan et al. (2017).

3.1 Selection of framework parameters

The model parameters are summarised in Table 2. The geometry and soil parameters were all known or measured, and are reported in Yuan et al. (2017). The critical state parameters were initially established by Stewart (1992) for the kaolin clay used in these model tests, and have since been adopted for numerical simulations of more recent model tests in the same clay kaolin clay (e.g. Feng & Gourvenec 2016; Chatterjee et al. 2013). $(s_u/\sigma'_{v0})_{NC}$ is quantified from the strength measured during initial penetration. For the Yuan et al. (2017) model tests, $(s_u/\sigma'_{v0})_{NC}$ = 0.16, from a ball penetrometer test using a bearing factor of 10.5 (Martin and Randolph, 2006) and a measured average effective soil unit weight, γ' = 6 kN/m^3. The ball penetrometer test also involved a cyclic remoulding phase, from which the soil sensitivity was estimated as S_t = 2.5.

For excess pore pressure generation, the parameters used in Equation 1 are the characteristic strain, ε_{99}, and the rate of excess pore pressure generation control parameter, p. These were established as ε_{99} = 100 and p = 2.6 in Zhou et al. (2018) by fitting the degradation of soil strength measured in a T-bar penetration test in normally consolidated UWA kaolin clay. For consolidation, the parameters used in Equation 3 are the dimensionless time for 50% consolidation, T_{50} and the embedment level parameter, m. These have been taken as T_{50} = 0.09, consistent with results from numerical analyses of an embedded pipeline reported by Chatterjee et al. (2013), and m = 1.4, higher than m = 1.05 in Chatterjee et al. (2013). This is selected because Chatterjee et al. (2013) showed that m increases with embedment depth, and the maximum SCR embedment depth is closer to one diameter rather than the maximum half

diameter in the Chatterjee et al. (2013) simulations. The coefficient of consolidation, c_v, was obtained from Rowe cell consolidation tests on UWA kaolin clay (House et al. 2001), where the dependence on vertical effective stress level, σ'_v, can be described as

$$c_v = \left(0.3 + 0.16\sigma'_v\right)^{0.47} \quad (14)$$

where c_v is in units of m^2/year and σ'_v is in kPa.

To define a shear strain influence zone and the strength influence zone for SCR tests, values of $\beta = 0.5$ and $\alpha = 0.5$ are selected, respectively, based on the clay failure mechanism for an SCR at shallow embedment (Randolph & White 2008a; Randolph & White 2008b), while for deep embedment, values of $\beta = 1$ and $\alpha = 1$ are selected, consistent with previous studies (Hodder et al. 2013, Zhou et al. 2018). The critical depth where the failure mechanism transfers from shallow to deep is taken here as $z/D = 2$, based on the shallow correction method outlined in White et al. (2010). It is assumed that β and α increase linearly from 0.5 at the mudline to unity at this critical depth.

The maximum stiffness used in Equation 8 was taken as $K_{max} = 200$, which is typical (Clukey et al. 2005, 2008, Randolph & Quiggin 2009) and corresponds to a soil rigidity ratio of $G_0/s_u \sim 300$ based on the relevant elastic and plastic solutions for half a diameter embedment (Guha et al. 2016, Randolph & White 2008b). The power parameter, ζ, in Equation 8 was taken as $\zeta = 0.32$ as this provided a good match with the measured mobilisation of soil resistance during T-bar penetration in normally consolidated kaolin clay (Zhou et al. 2018). In summary, all model parameters are either derived from the strength profiles determined in Yuan et al. (2017), or have been calibrated in previous studies, and are initially applied here without modification, before further improvements are examined.

3.2 Results and Discussion

3.2.1 Short-term SCR test

The framework calculates changes in seabed strength, which is then linked to seabed resistance, q_s, through Equation 11, providing a prediction of the resistance during the vertical motion (Figure 6). As noted earlier in the paper, soil buoyancy, q_b, is included, making allowance for soil heave through the factor f_b in Equation 12. For soft clay, f_b may be taken as 1.3, reducing to unity at the critical depth of $\hat{z} = 2$, consistent with previous studies (Merifield et al. 2009). The SCR penetration resistance is the sum of $q_s(\hat{z})$ and $q_b(\hat{z})$ at each soil horizon, via Equation

10.

Figure 7 compares the model simulations and the measurements for the short-term test. Negative values of penetration resistance correspond to a downwards geotechnical resistance on the SCR, which is created when the SCR moves upwards. The cyclic strength degradation is illustrated in Figure 7a, which shows the ratio of the seabed penetration resistance at cycle number N to that in the first cycle, $q_{s,N}/q_{s,1}$, at a normalised depth, $\hat{z} = 2$. The measurements show that the seabed penetration resistance gradually degrades to $q_{s,N}/q_{s,1}$ ~0.25 after about 200 cycles, lower than the simulations which provide a steady-state $q_{s,N}/q_{s,1}$ ~0.42 at $N = 200$, close to $1/S_t$ as expected for a fully remoulded condition. However, and as noted in Yuan et al. (2017), a lower penetration resistance is to be expected for this 'mudline-breaking' test, where the continued passage of the SCR across the water-mudline interface allowed water to become entrained at the SCR-seabed interface.

This water entrainment leads to a mobilised soil strength that is lower than the nominally remoulded soil strength (e.g. that would be measured in a cyclic penetrometer test), as also noted in cyclic 'mudline-penetrating' SCR and T-bar penetrometer tests (e.g. Clukey et al. 2005; Hodder et al. 2009; Gaudin and White 2009), and experimental studies on suction caissons (e.g. Gaudin et al. 2014), dynamically installed anchors (e.g. Richardson et al. 2009, O'Beirne 2017) and in high-rate ring-shear tests (where water was permitted to penetrate the shear zone, Tika and Hutchinson, 1999). The RSL defines the fully remoulded state in the framework, and S_t is the primary parameter that controls the position of the RSL through Equation 2. To account for the effect of water entrainment, S_t is raised, shifting the RSL to the left, which results in a lower effective stress, and therefore strength, after remoulding.

In order to capture the additional loss in seabed strength from the water entrainment, values of $S_t = 4$, $\varepsilon_{99} = 600$ and $p = 2.95$ are used to match the experimental measurements, in which the higher S_t represents a lower (water entrained) remoulded soil strength; the higher ε_{99} requires a greater level of strain to reach the fully softened condition through water entrainment, and p is modified to ensure that the calculated initial shear strength gradient agrees with the measured ~0.96 kPa/m. The revised simulations are also shown in Figure 7a and are in good agreement with the experimental measurements.

Figure 7b compares simulated and measured (depth) profiles of SCR penetration resistance, q, at cycle numbers N = 1, 2, 50 and 200, using the modified parameters that represent water entrainment. The gradient of resistance with depth reduces at $\hat{z} = 1$, which is due to the non-

linear increase in soil buoyancy as the SCR becomes fully embedded (i.e. over $\hat{z} \leq 1$). Soil buoyancy is an upwards positive resistance of approximately 5 kPa for $\hat{z} > 1$, which results in (the fully embedded) q between penetration and extraction being approximately symmetrical about this offset. Figure 7b shows that the framework is capable of capturing accurately the loss in both the penetration and extraction resistance during the initial 200 cycles of penetration. Over this period consolidation effects are negligible.

3.2.2 Long-term SCR test

3.2.2.1 Modelling of the open trench

Simulations of the long-term test required that the experimental observations of a developing open trench were accounted for in the simulations, as an additional input. As shown in Figure 8, the trench depth, z_{trench}, in the experiments increased with cycle number, reaching a temporarily stable $z_{trench}/D \sim 0.18$ after $N = 200$, before increasing to $z_{trench}/D \sim 0.67$ after the complete set of $N = 3{,}000$ cycles. The initial trench formation to about 0.18 times the SCR diameter is due to the lateral displacement of soil associated with the repeated passage of the SCR through the mudline. This results in heave at the mudline adjacent to the SCR, and a depression at the SCR location. The continued deepening of the trench is due to the gradual reduction in specific volume of the penetrated column of soil due to consolidation.

The evolving trench was accounted for in the simulations by defining an effective penetration depth, $z' = z\text{-}z_{trench}$, where z is the SCR penetration depth relative to the original mudline as defined earlier. Soil buoyancy is then calculated using the effective penetration depth, and values of $q_b = 0$ and $q_s = 0$ are assigned when the SCR is below the original mudline but still above the current soil surface, i.e. for $z' \leq 0$.

3.2.2.2 Variation in SCR penetration resistance

Figure 9 compares the simulated and measured resistance profiles at different cycles. In this test the SCR was penetrated until $q = 8$ kPa, such that the maximum penetration resistance is similar in each profile, but is reached at different embedment depths at cycle number increases. Over the first 100 cycles (Figure 9a-d) the penetration depth at which $q = 8$ kPa increases, reflecting the remoulding and water entrainment processes that reduce soil strength. However, at higher cycle numbers (N = 1,000 to 3,000; Figure 9e-h) the limiting penetration depth reduces as the soil strength increases through consolidation.

Over the first 100 cycles, the simulations are in remarkable agreement with the measurements for both penetration and extraction. At higher cycle numbers, the model captures well the limiting embedment depth, whilst slightly over-predicting q during penetration at shallow embedment. However, q during extraction is overestimated in the simulations at the higher cycle numbers. The simulated extraction resistance is approximately symmetrical about the soil buoyancy resistance profile as for any given cycle the calculated seabed resistance, q_s, is equal for penetration and extraction. This is consistent with the steady-state that is reached during the cyclic remoulding phase of a full-flow penetrometer test, or indeed the transient steady-state resistance that was reached during the short-term SCR test on Figure 7a, which is why the simulations are in good agreement with both the measured penetration and extraction q profiles over the first 100 cycles on Figure 9.

The much lower measured extraction q (relative to penetration) at higher cycle numbers indicates that other processes are involved during extraction. As the SCR reverses direction from penetration to extraction, q initially becomes lower than q_b indicating that some reverse bearing capacity is mobilised (although by a small amount relative to the difference between q and q_b during penetration). However, it appears that this resistance is rapidly lost, perhaps because suction cannot be mobilised if free water can reach the interface around the invert of the SCR. Thereafter, the uplift resistance is approximately equal to q_b for the remainder of the extraction. Whilst the framework does not capture this effect, the calculated SCR-seabed stiffness is unaffected as this is based solely on the penetration response.

3.2.2.3 Variation in effective stress state and soil strength

The internal variables of the simulation shown in Figure 9 allow the changes in effective stress and strength during the long-term test to be illustrated. Figure 10 presents the variation in calculated effective stress state and corresponding changes in undrained shear strength at $z'/D = 0.4$ over the 3,000 cycles. A number of features are observed:

- During the first few cycles of penetration, the excess pore pressure generation is much higher than the excess pore pressure dissipation, such that the vertical effective stress state approaches the RSL.
- As the SCR motion is continuous, the effective stress state changes only slightly between each cycle as there is a very short reconsolidation period between the shearing events. Consequently, the effective stress path tracks close to the RSL, although closer inspection (inset in Figure 10a) reveals that each cycle is associated with a small

459 increase in vertical effective stress along the URL with the corresponding reduction in
460 specific volume.

461 • As the cycle number increases, so too does the vertical effective stress on the RSL, such
462 that the potential for maximum excess pore pressure generation, $u_e = \sigma'_{v,eqm} - \sigma'_{v,RSL}$,
463 progressively decreases from a maximum u_e ~2.2 kPa at the start of the test to u_e ~ 0.3
464 kPa at N = 3,000. The 3,000 cycles involve a duration, t ~ 16 hours at model scale
465 (equivalent to ~ 4.6 years at prototype scale), which corresponds to a dimensionless time,
466 $T = c_v t/D^2$ ~ 4 (adopting c_v ~ 0.85 m^2/year for σ'_v = 2.4 kPa at a normalised depth of
467 z'/D = 0.4, via Equation 14). Hence, the remaining excess pore pressure after 3,000
468 cycles, at T ~ 4, is equivalent to ~14% of the initial maximum excess pore pressure. By
469 way of comparison, the elastic solution for 90% dissipation for a pipeline under a
470 maintained load at an embedment of z'/D = 0.5 is T_{90} ~2 (Gourvenec & White, 2010),
471 and an elasto-plastic solution for the same case is T_{90} ~0.7 (Chatterjee et al. 2013). The
472 higher T to approach equilibrium in these simulations is because pore pressure is being
473 successively generated and dissipated to reach the densified state where limited further
474 pore pressure can be generated. In contrast, the conventional dissipation solutions
475 indicate the time required for a single dissipation event.

476 • Figure 10b shows the change in undrained shear strength at z'/D = 0.4 over the 3,000
477 cycles. The strength decreases (by a factor of ~S_t) from an initial value of s_u = 0.4 kPa
478 at N =1 to s_u = 0.13 kPa at N = 50, due to the generation of excess pore pressure with
479 practically no consolidation induced reduction in specific volume (as shown by Figure
480 10a). Over the remaining 2,500 cycles s_u increases to ~ 1.2 kPa, with an extended
481 analysis to N = 10,000 giving s_u ~ 1.4 kPa, which corresponds to ~99% consolidation.
482 Hence, the (near) limiting undrained shear strength is approximately 3.5 times the initial
483 value, identical to the ratio of drained to undrained strength for UWA kaolin clay as
484 inferred from penetrometer tests (Colreavy et al. 2016).

485 **3.2.2.4 Variation in seabed penetration stiffness**

486 As noted earlier in the paper, a key design issue for assessing the fatigue life of an SCR at the
487 TDZ is selecting an appropriate value for the SCR penetration stiffness, k_s, given by

488 $$k_s = \frac{q_{max}}{z'} \quad (15)$$

489 where q_{max} is the maximum SCR penetration resistance during each cycle of penetration linked

to the (changing) soil strength through Equation 10 and 11.

Figure 11 compares the simulated and measured evolution of penetration stiffness with cycle number. Both the experimental and simulated result include some scatter as the achieved limiting pressure varied slightly between cycles, in the range q_p = 8 to 10 kPa. The simulations in Figure 12 used same limiting value of q_p for each cycle as in the experiments. The initial reduction in stiffness over the first ~100 cycles reflects the lower soil strength due to remoulding. This stiffness is regained as the soil strength increases through consolidation, with final values of k_s that are approximately 1.8 times the initial value. This trend is captured well by the simulations.

To illustrate the sensitivity of the response to the extent that the soil softens due to water entrainment, additional simulations were conducted using different values of S_t = 2.5, 4 and 10 with a constant applied pressure, q_p = 8 kPa, for 10,000 cycles. The results are summarized in Figure 12, and show that although S_t affects k_s in the short term (over the first 200 cycles) by calculating a lower soil strength, the long-term response results in limiting values of k_s that are independent of S_t. This is a useful finding as it emphasizes that the long-term stiffness – most relevant to fatigue – is independent of the water entrainment, so that quantifying this effect is a low priority.

4. FIELD SCALE EXAMPLE ANALYSES

The simulations described above show that the effective stress framework can capture the influence of both remoulding and consolidation, to replicate the changes in strength and stiffness that occur during centrifuge tests that involve both effects. The framework is therefore a useful tool to evaluate the relative influence of remoulding and consolidation on the long-term SCR-seabed stiffness, which has a significant influence on fatigue life, which is explored in this closing section.

A particular benefit of the framework is that it allows the response to be scaled from the centrifuge tests conditions to field conditions, where the relative rates of cycling and consolidation are very different. In centrifuge tests, apparatus limitations prevent the motion cycles being performed at a frequency that matches the rate at which pore pressure dissipation is accelerated – which is N^2, where N is the centrifuge acceleration. In the centrifuge tests of Yuan et al (2017), N = 50, so dissipation processes were accelerated by 2,500 times relative to field conditions. However, the motion cycles had a period of approximately 1 second in the long-term test, relative to a field oscillation frequency that would be in the order of 10 seconds,

so were accelerated only by a factor of 10. An alternative way to express this is that in the field, 250 times more cycles would occur in the same period of pore pressure dissipation that was modelled in the centrifuge tests. This scaling mismatch means that the relative contributions of remoulding and consolidation may not be correct, and an unrealistically high level of consolidation is associated with a given number of cycles in the centrifuge.

This limitation of the centrifuge test is overcome using the framework, which allows the effects of remoulding and consolidation on long term seabed stiffness to be evaluated, with the confidence that the model parameters are calibrated to the centrifuge tests. A set of twelve simulations were conducted using the parameters given in Table 3. These parameters were chosen to represent normally consolidated soft clay in Gulf of Mexico, where SCRs are widely used. The simulations adopted an SCR diameter, D = 0.5 m and an applied pressure, q_p = 4 kPa, considered representative for soft seabeds (Shiri, 2010). Summarised in Table 4, the twelve simulations are arranged into three groups, all with a penetration 'limit' of q_p = 4 kPa, but with the same four variations on extraction limits for each cycle. These were extraction to q_p = 1 kPa, and extraction by displacements of 0.0025D, 0.025D and 0.25D. Each group considered two orders of magnitude variation in the coefficient of consolidation, (c_v = 1, 10 and 100 m^2/year) to explore the time scales over which the SCR stiffness changes.

In practice, at a given location in an SCR touchdown zone, the penetration stress limit may reduce with cycles as a trench forms and the concentrated vertical load spreads along the touchdown zone. This may reduce the trenching and stiffening effect seen at that point, but will raise the effect seen at adjacent points.

Example results from the simulations are provided in Figure 13, which shows the variation in SCR penetration resistance against normalised effective penetration depth for cases 2, 6 and 10 (c_v = 1, 10 and 100 m^2/year, respectively, and an uplift displacement of 0.025D).. Consistent with the observations from the Yuan et al. (2017) centrifuge tests, the cyclic hysteresis loop becomes deeper over the first N = 1,000 cycles as the soil progressively remoulds, but then becomes shallower due to consolidation-induced increases in soil strength, and a higher c_v results in a quicker regain in soil strength and SCR penetration resistance.

Figure 15 shows the variation in SCR-seabed stiffness with cycle number for the c_v = 10 m^2/year simulations. The stiffness adopted is an unloading secant stiffness, K_{sec}, defined in Figure 14 as

$$K_{sec} = \triangle q_s / \triangle z = (q_s - q_{s,rev})/(\hat{z} - \hat{z}_{rev}) \quad (16)$$

where $q_{s,rev}$ and $\hat{z}_{rev}$ are the seabed resistance and normalised penetration depth corresponding to the last point of load reversal. Figure 15 shows the expected reduction in K_{sec} with normalised cyclic displacement, $\triangle z/D$, and also the trend of reducing and then increasing K_{sec} with cycle number, associated with initial softening and then consolidation-induced hardening of the soil. The degradation of secant stiffness can also be captured by existing SCR-seabed stiffness models, as demonstrated in Figure 15 by the Aubeny et al. (2015) model using parameters that lead to the same amount of softening behaviour over the same loading period as the current model. However, those models do not predict the regain in the stiffness due to consolidation, so they predict a long-term stiffness that is much lower than the eventual value.

Figure 16 presents the evolution of secant stiffness at a cyclic displacement of $\triangle z/D = 0.002$. The results are shown against cycle number, N, and time, t, on Figure 16a and against dimensionless time, T, on Figure 16b. As indicated by Figure 15, the simulations capture both the initial reduction and subsequent increase in stiffness. The rate of stiffness reduction is controlled by the cyclic displacement adopted for each cycle, such that at low cycle numbers the simulations group according to the cyclic displacement and are independent of c_v.

In contrast, the increase in stiffness is controlled by the consolidation duration, such that at larger cycle numbers the simulations group according to c_v. Stiffness eventually stabilises at cycle numbers and durations that depend on c_v; the c_v = 100 m^2/year cases stabilise after 1.5 months ($N = 3.5 \times 10^5$), the c_v = 10 m^2/year cases stabilise after 3.2 years ($N = 1 \times 10^7$) and the c_v = 1 m^2/year cases stabilise after 60 years ($N = 2 \times 10^8$). Hence, for a typical design life of 30 years, the SCR-seabed stiffness for the majority of the life is the long-term steady-state fully-reconsolidated stiffness, except for seabed with c_v = 1 m^2/year, for which the SCR-seabed stiffness is 55%, 75% and 90% of the stabilised (and maximum) K_{sec} after 10, 20 and 30 years, respectively.

The use of dimensionless time, T, in Figure 16b tends to eliminate the influence of c_v, although some dependence remains during the early stages as the higher c_v cases reach a state in which cycles do not generate any pore pressure more quickly, and during the consolidation stage the deviation of $K_{sec}/q_{s,i}$ between the three c_v groups is affected by the SCR embedment depth. This is because the soil horizons at different depths experienced different remoulding at the same T, which results in a different ratio between $q_s/q_{s,i}$. For example, on Figure 13, the cycles at $T \sim 10$ are highlighted for the cases with different values of c_v , showing the difference in embedded depth and therefore $q_{s,i}$ at the same dimensionless time. However, all the simulations approach

586 the same stabilised depth and stiffness, and this gain in stiffness was 50% complete at a
587 dimensionless time of $T\sim 10$ on average. For these example cases, this stiffness is about 3 times
588 higher than the initial stiffness and ~10 times higher than would be predicted as the steady-state
589 remoulded value assumed in current SCR-seabed stiffness models.

590 ## 5. CONCLUSIONS

591 Compared with current published models and design practice, in which SCR-seabed interaction
592 is analysed using a total stress approach ignoring any influence of drainage of pore water
593 pressure, the analysis proposed in this paper shows a significant improvement. Three important
594 contributions are made: (1) the new method uses an effective stress framework, and is defined
595 with sufficient generality to allow realistic simulation of 'whole-life' cyclic loading histories.
596 This unlocks the 'hidden' effect of consolidation on soil strength and stiffness, rather than using
597 a predefined empirical factor applied to the intact soil strength and resistance, as is current
598 practice; (2) it proposes a sound theory that captures the experimental observations, allowing
599 reliable prediction of changes in penetration resistance and stiffness through remoulding and
600 reconsolidation – including extrapolation from centrifuge tests to arbitrary field conditions; (3)
601 many of the model parameters are derived from full-flow penetrometer test data, so it provides
602 the potential to bridge between in situ tests and SCR design predictions.

603 A series of simulations are presented to illustrate a range of typical field scenarios, and show
604 the progressive rise in stiffness during continuous cycling motion, due to consolidation. It is
605 shown that current design practice may underestimate the seabed stiffness significantly, but the
606 new approach allows rapid checking of this for particular combinations of SCR and soil
607 conditions.

608 ## 6. ACKNOWLEDGEMENTS

609 The first author acknowledges his research studentship support from the ARC Industrial
610 Transformation Research Hub for Offshore Floating Facilities and the University of Western
611 Australia. This work was supported by the ARC Industrial Transformation Research Hub for
612 Offshore Floating Facilities which is funded by the Australia Research Council, Woodside
613 Energy, Shell, Bureau Veritas and Lloyds Register (Grant No. IH140100012).
614

615

7. NOTATION

b	peak strength parameter, $k_\Phi(\hat{z}) = OCR(\hat{z})^b$
c_v	coefficient of consolidation
D	diameter of penetrating SCR
K	tangent stiffness
K_{max}	maximum tangent stiffness adopted since the last reversal in penetration or extraction
m	parameter for dissipation rate
N_c	bearing capacity factor
p	parameter for pore pressure generation rate
q	SCR penetration resistance
q_s	seabed resistance
q_p	applied pressure
s_u	undrained shear strength
$s_u(\bar{z})$	undrained shear strength profile
$s_{u,i}$	in-situ undrained shear strength
$s_{u,av}$	average undrained shear strength
$s_{u,c}$	consolidated soil strength
$s_{u,cyc}$	cyclic undrained shear strength
$s_{u,mob}$	mobilised soil strength
S_t	soil sensitivity
$\left(\frac{s_u}{\sigma'_{v0}}\right)_{NC}$	normally consolidated undrained strength ratio
t	reconsolidation period

T	dimensionless time factor
T_{50}	dimensionless time factor required for 50% dissipation of the initial excess pore pressure
U	degree of dissipation
$u_{\mathrm{e}}(\bar{z})$	excess pore pressure profile
$u_{\mathrm{e,r}}(\bar{z})$	remaining potential excess pore pressure profile
$u_{\mathrm{e,max}}(\bar{z})$	maximum excess pore pressure profile
$v_{\mathrm{s}}(\hat{z})$	strength influence function
v_{p}	penetration velocity of the object
v	specific volume
v_{initial}	initial specific volume
z	soil depth
$\hat{z}$	normalised soil depth, z/D
z_{m}	depth of reference point of penetrating object below soil surface
$\hat{z}_{\mathrm{m}}$	normalised depth, z_{m}/D
α	strength influence zone extent
β	strain influence zone extent
χ	characteristic pressure
η	load sharing factor
λ	gradient of the normal consolidation line (NCL)
κ	gradient of the unload-reload line (URL)
Φ	lumped strength parameter
Φ_{steady}	steady value of lumped strength parameter
k_{Φ}	strength parameter multiplier

σ'_v	vertical effective stress
$\sigma'_{v,eqm}$	equilibrium vertical effective stress
$\sigma'_{v,NCL}$	vertical effective stress at NCL
$\sigma'_{v,RSL}$	vertical effective stress at RSL
σ'_{v0}	in situ geostatic effective stress
ε	cumulative (absolute) shear strain
ε_{99}	cumulative (absolute) shear strain required for a degree of remoulding equal to 99%
$\varepsilon_{95,\Phi}$	peak strength ductility parameter
$\mu(\hat{z})$	strain influence distribution function
Ψ	vertical distance between the object penetration depth and a given soil horizon normalised by the object diameter
Λ	plastic volumetric strain ratio
Γ_{NCL}	specific volume, v, σ'_v = 1 kPa on the NCL
ζ	nonlinear tangent stiffness parameter
γ'	soil effective unit weight

8. REFERENCES

Aubeny, C. and Biscontin, G. (2009). Seafloor-riser interaction model. *International Journal of Geomechanics*, 9(3), 133–144.

Aubeny, C., Gaudin, C. and Randolph, M.F. (2008). Cyclic tests of model pipe in kaolin. In *Proceedings of the Offshore Technology Conference (OTC)*, Houston, Paper no. OTC19494.

Bridge, C., Laver, K., Clukey, E. and Evans, T. (2004). Steel catenary riser touchdown point vertical interaction models. In *Proceedings of the Offshore Technology Conference (OTC)*, Houston, Texas, USA, Paper no. OTC16628.

Clukey, E.C., Haustermans L. and Dyvik R. (2005). Model Tests to Simulate Riser-Soil Interaction in Touchdown Point Region. In *Proceedings of the International Symposium on Frontiers in Offshore Geotechnics*, Perth, Australia, 651–658.

Clukey, E.C., Young, A.G., Dobias, J.R. and Garmon, G.R. (2008). Soil response and stiffness laboratory measurements of SCR pipe/soil interaction. In *Proceedings of the Offshore Technology Conference (OTC)*, Houston, Texas, USA, Paper no. OTC19303.

Clukey, E. C. and Zakeri, A. (2017). Recent Advances in Nonlinear Soil Models for Fatigure Evaluation of Steel Catenary Risers SCRs. In *Proceedings of the Offshore Technology Conference (OTC)*, Houston, Texas, USA, Paper no. OTC27627.

Clukey E. C., Aubeny C. P., Randolph M. F., Sharma P. P., White D. J., Sancio R. and Cerkovnik M. (2017). A Perspective on the State of Knowledge Regarding Soil-Pipe Interaction for SCR Fatigue Assessments. In *Proceedings of the Offshore Technology Conference (OTC)*, Houston, Texas, USA, Paper no. OTC27564.

Chatterjee, S., White, D. J. and Randolph, M. F. (2013). Coupled consolidation analysis of pipe-soil interactions. *Canadian Geotechnical Journal*, 50(6), 609–619.

Cocjin, M. L., Gourvenec, S. M., White, D. J. and Randolph, M. F. (2017). Theoretical framework for predicting the response of tolerably mobile subsea installations. *Géotechnique*, 67(7), 608–620.

Colreavy, C., O'Loughlin, C. D. and Randolph, M. F. (2016). Experience with a dual pore pressure element piezoball. *International Journal of Physical Modelling in Geotechnics*,

16(3), 101–118.

Elosta, H., Huang, S. and Incecik, A. (2013). Dynamic response of steel catenary riser using a seabed interaction under random loads. *Ocean Engineering*, 69, 34–43.

Elosta, H., Huang, S. and Incecik, A. (2014). Trenching effects on structural safety assessment of integrated riser/semisubmersible in cohesive soil. *Engineering Structures*, 77, 57–64.

Einav, I. and Randolph, M. F. (2005). Combining upper bound and strain path methods for evaluating penetration resistance. *International Journal for Numerical Methods in Engineering*, 63(14), 1991–2016.

Feng, X. and Gourvenec, S. (2016). Modelling sliding resistance of tolerably mobile subsea Mudmats. *Géotechnique* 66(6):1-10.

Gaudin, C., O'Loughlin, C.D., Hossain, M.S. and Colliat J-.L. (2014). Suction caisson installation and performance in Angola clay. In *Proceedings of the 8th International Conference on Physical Modelling in Geotechnics*, Perth, Australia, 493–399.

Gourvenec, S.M., and White, D.J. 2010. Elastic solutions for consolidation around seabed pipelines. *In Proceedings of the Offshore Technology Conference (OTC)*, Houston, Texas, USA, Paper no. OTC20554.

Guha, I., Randolph, M. F. and White, D. J. (2016). Evaluation of Elastic Stiffness Parameters for Pipeline–Soil Interaction. *Journal of Geotechnical and Geoenvironmental Engineering*, 142(6).

Hodder, M. White, D. J. and Cassidy, M. J. (2009). Effect of remolding and reconsolidation on the touchdown stiffness of a steel catenary riser: Observations from centrifuge modelling. In *Proceedings of the Offshore Technology Conference (OTC)*, Houston, Texas, USA, Paper no. OTC19871.

Hodder, M. S., White, D. J. and Cassidy, M. J. (2013). An effective stress framework for the variation in penetration resistance due to episodes of remoulding and reconsolidation. *Géotechnique*, 63(1), 30–43.

Hou, Z., Sahdi F., Gaudi C. & Randolph M.F. (2018). Evolution of riser-soil stiffness in a soil crust layer. *Proc. Vietnam Symposium on Offshore Engineering*. Springer 130-136.

House, A., Olivera, J. R. M. S. and Randolph, M. F. (2001). Evaluating the coefficient of

675 consolidation using penetration tests. *International Journal of Physical Modelling in*
676 *Geotechnics*, 3, 17–25.

677 Kimiaei, M., Randolph, M. F. and Ting, I. (2010). A parametric study on effects of
678 environmental loadings on fatigue life of steel catenary risers (using a nonlinear cyclic
679 riser-soil interaction model). In *Proceedings of the 29th International Conference on*
680 *Ocean, Offshore and Arctic Engineering*, Shanghai, China, Paper no. OMAE2010-21153.

681 Li, F. Z. and Low, Y. M. (2012). Fatigue reliability analysis of a steel catenary riser at the
682 touchdown point incorporating soil model uncertainties. *Applied Ocean Research*, 38, 100
683 –110.

684 Merifield R. S., White D. J. and Randolph M. F. (2009). Effect of surface heave on the response
685 of partially embedded pipelines on clay. *Journal of Geotechnical and Geoenvironmental*
686 *Engineering*, 135(6), 1–11.

687 Martin, C. M. and Randolph, M. (2006). Upper-bound analysis of lateral pile capacity in
688 cohesive soil. *Géotechnique*, 56(2), 141–145.

689 O'Beirne, C., O'Loughlin, C. D. and Gaudin, C. (2017). Assessing the penetration resistance
690 acting on a dynamically installed anchor in normally consolidated and overconsolidated
691 clay. *Canadian Geotechnical Journal*, 54(1), 1–17.

692 Queau, L. M., Kimiaei, M. and Randolph, M. F. (2013). Dimensionless groups governing
693 response of steel catenary risers. *Ocean Engineering*, 74, 247–259.

694 Randolph, M.F. and Hope, S.N. (2004). Effect of cone velocity on cone resistance and excess
695 pore pressure. Proc. Conf. on Engineering Practice and Performance of Soft Deposits,
696 Osaka, 147-152.

697 Randolph, M. F. and White, D. J. (2008a). Pipeline embedment in deep water: processes and
698 quantitative assessment. In *Proceedings of the Offshore Technology Conference (OTC)*,
699 Houston, Texas, USA, Paper no. OTC19128.

700 Randolph, M. F. and White, D. J. (2008b). Upper bound yield envelopes for pipelines at shallow
701 embedment in clay, *Géotechnique* 58(4), 297–301.

702 Randolph, M. F. and Quiggin P. (2009). Non-linear hysteretic seabed model for catenary
703 pipeline contact. In *Proceedings of the 28th International Conference on Ocean, Offshore*

and Arctic Engineering, Honolulu, Hawaii, USA, Paper no. OMAE2009-79259.

Richardson, M. D., O'Loughlin, C. D., Randolph, M. F. and Gaudin C. (2009). Setup Following Installation of Dynamic Anchors in Normally Consolidated Clay. *Journal of Geotechnical and Geoenvironmental Engineering*, 135(4), 487–496.

Shiri, H. (2010). Influence of seabed response on fatigue performance of steel catenary risers in touchdown zone. Ph.D thesis, the university of Western Australia.

Stewart, D. P. and Randolph, M. F. (1991). A new site investigation tool for the centrifuge. In *Proceedings of the International Conference on Centrifuge Modelling, Centrifuge '91*, Boulder, Colorado, USA, 531–538.

Stewart, D. P. (1992). Lateral loading of piled bridge abutments due to embankment construction. PhD thesis, The University of Western Australia, Perth, Australia.

Sahdi, F., White, D. J., Gaudin, C., Randolph, M. and Boylan, N. (2015). Laboratory development of a vertically oriented penetrometer for shallow seabed characterization, *Canadian Geotechnical Journal*, 53(1), 93–102.

Tika Th. E. and Hutchinson J. N. (1999). Ring shear tests on soil from the Vaiont landslide slip surface. *Géotechnique*, 49(1), 59–74.

Voie, P. E., Skeie, G. and Bergan-Haavik, J. (2014). Importance rating of riser-soil interaction effects. In *Proceedings of the 33rd International Conference on Ocean, Offshore and Arctic Engineering*, San Francisco, California, USA, Paper no. OMAE2014-24179.

White D. J., Gaudin, C., Boylan, N. & Zhou H. (2010). Interpretation of T-bar penetrometer tests at shallow embedment and in very soft soils. *Canadian Geotechnical Journal*, 47(2), 218–229.

White D. J. and Hodder M. (2010). A simple model for the effect on soil strength of episodes of remoulding and reconsolidation. *Canadian Geotechnical Journal*, 47(7), 821–826.

Yuan, F., White, D. J., and O'Loughlin, C. D. (2017). The evolution of seabed stiffness during cyclic movement in a riser touchdown zone on soft clay. *Géotechnique*, 67(2), 127-137.

You, J., Biscontin, G., and Aubeny, C. P. (2008). Seafloor Interaction with Steel Catenary Risers. In *Proceedings of the 8th International Offshore and Polar Engineering Conference*, Vancouver, British Columbia, Canada, Paper no. ISOPE-I-08-303.

Zargar, E. (2017). A new hysteretic seabed model for riser-soil interaction. PhD thesis, The University of Western Australia, Perth, Australia.

Zhou Z., White D. J. and O'Loughlin, C. D. (2018). An effective stress framework for estimating penetration resistance accounting for changes in soil strength from maintained load, remoulding and reconsolidation. *Géotechnique,* in press, doi:10.1680/jgeot.17.P217.

9. FIGURE CAPTIONS

10. TABLE CAPTIONS

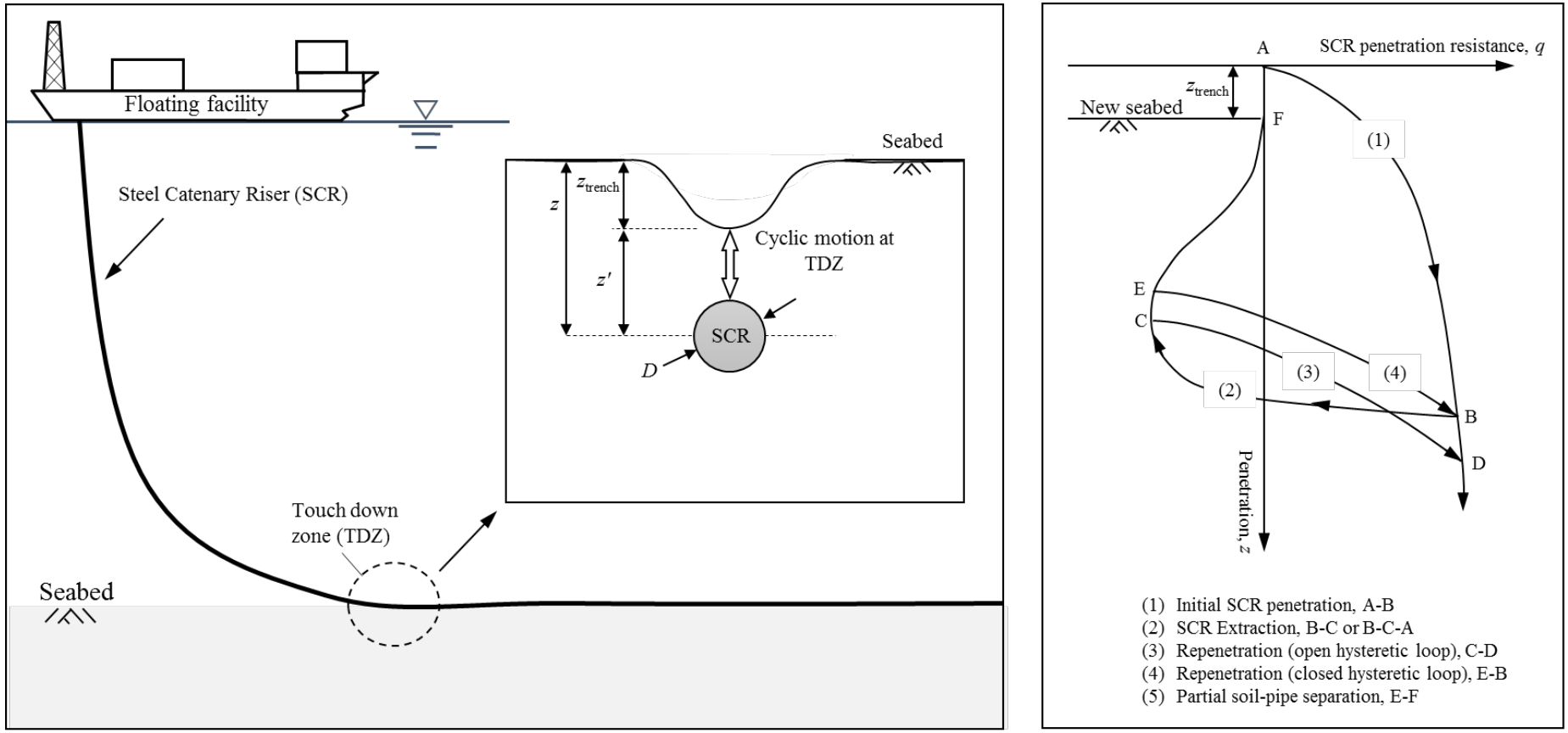

(a) (b)

Figure 1 Steel catenary risers: (a) problem definition and notation; (b) typical soil response during vertical cyclic motion (after Aubeny and Biscontin, 2009)

798

799

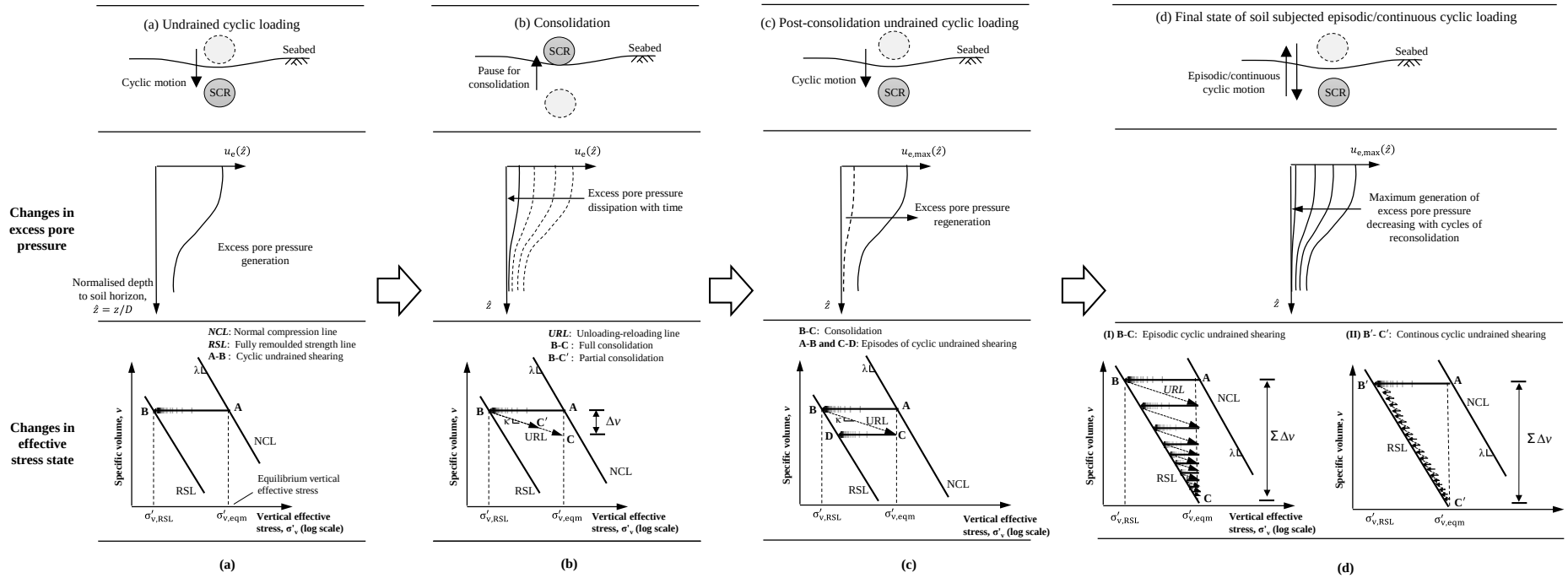

Figure 2 Variation in vertical effective stress state and excess pore pressure during different scenarios: (a) undrained cyclic loading; (b) consolidation process; (c) subsequent undrained cyclic loading; (d) progression of soil state during episodic or continuous cyclic loading

800

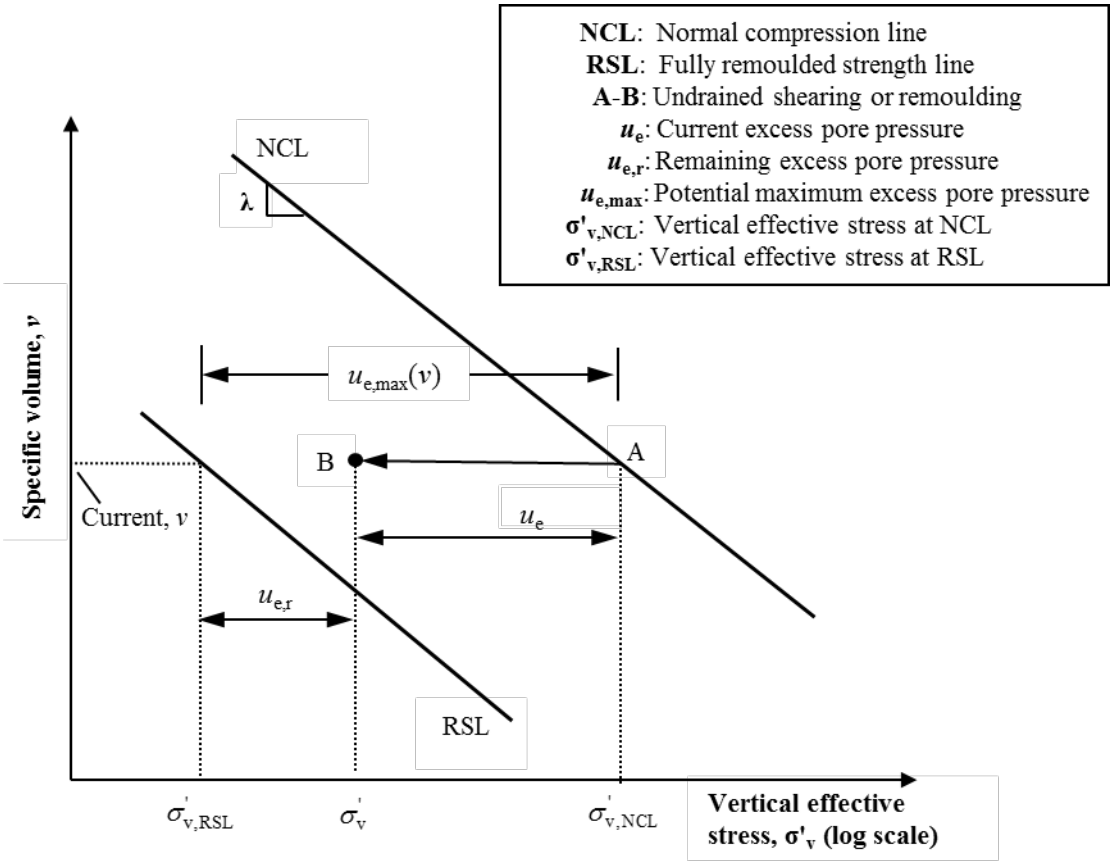

Figure 3 Definition of maximum excess pore pressure (after Zhou *et al.* 2018)

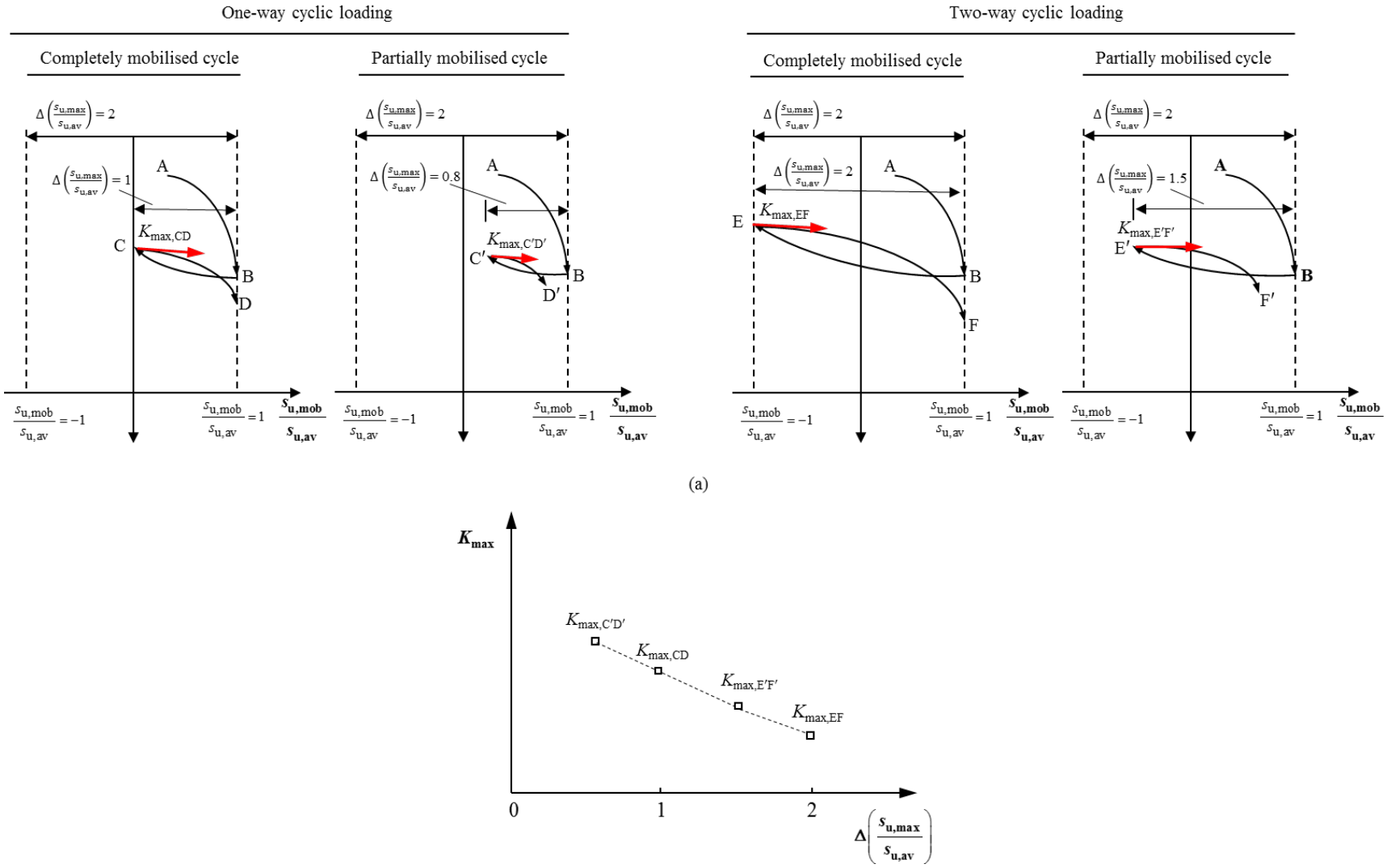

Figure 4 Mobilisation of soil strength under complex motion: (a) complete and partial cycles under one-way and two-way cyclic loading; (b) corresponding maximum tangent stiffness

826

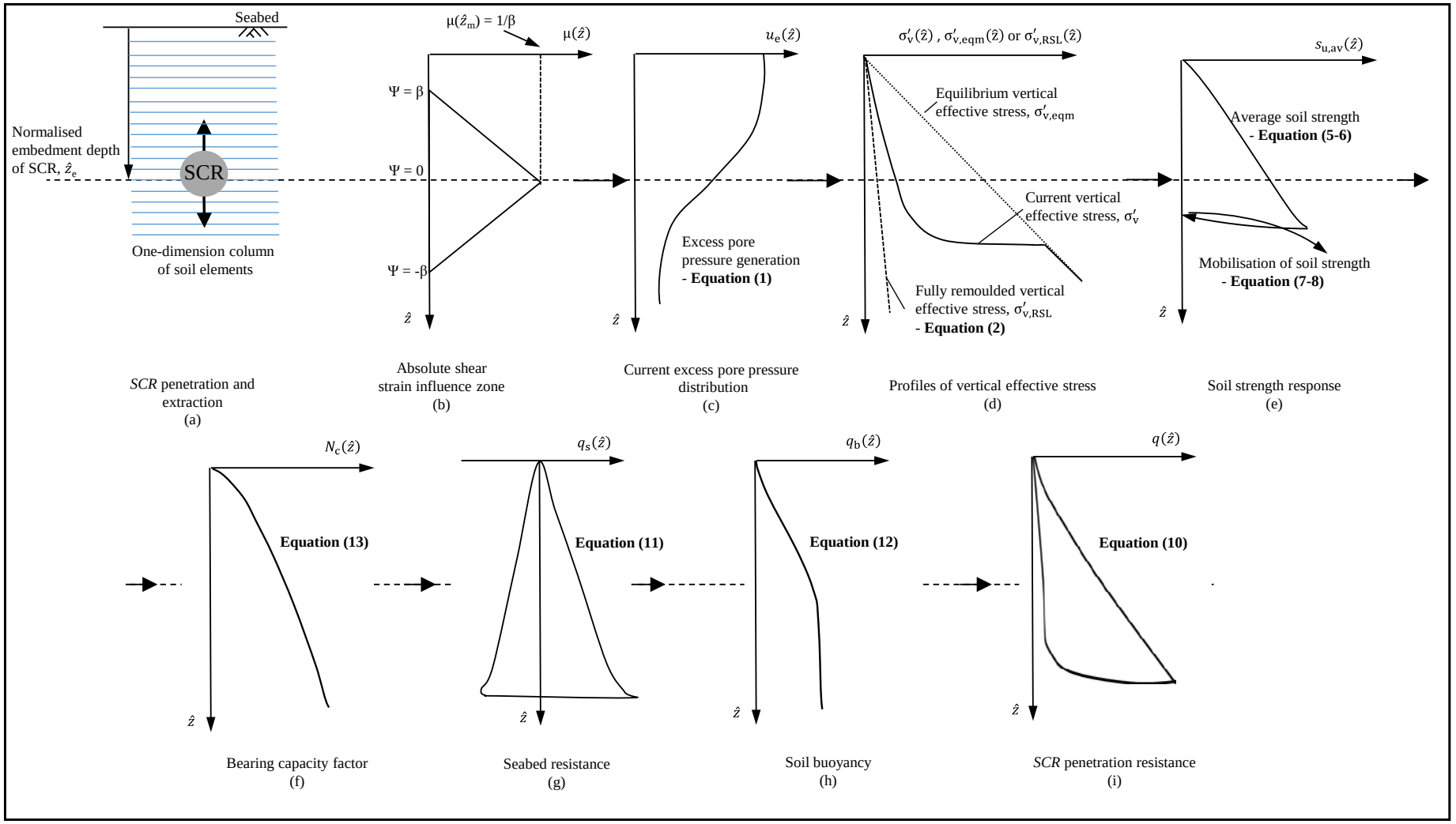

Figure 5 Schematic representation of the one-dimensional effective stress framework applied to SCR-seabed interaction

827

828

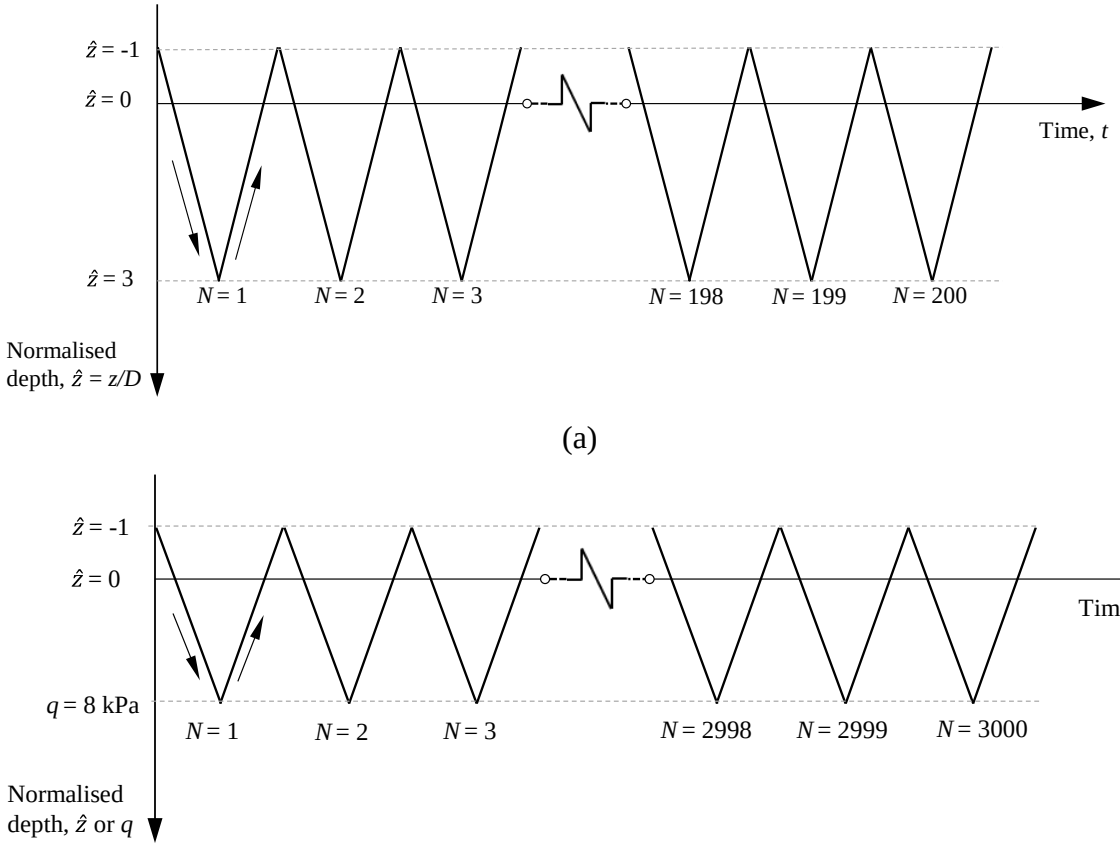

Figure 6 Displacement – time histories of: (a) short-term SCR test; (b) long-term SCR test (from Yuan et al. 2017)

829

830

831

832

833

834

835

836

837

838

839

840

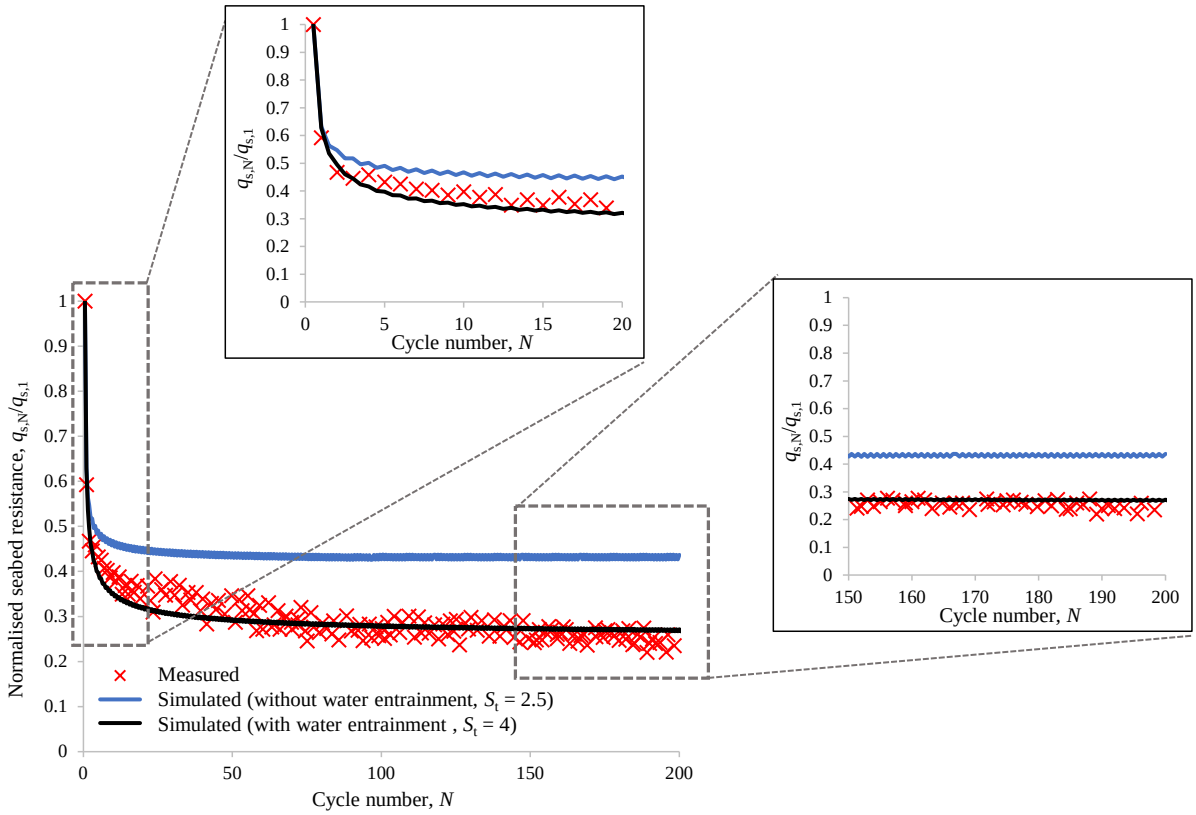

(a)

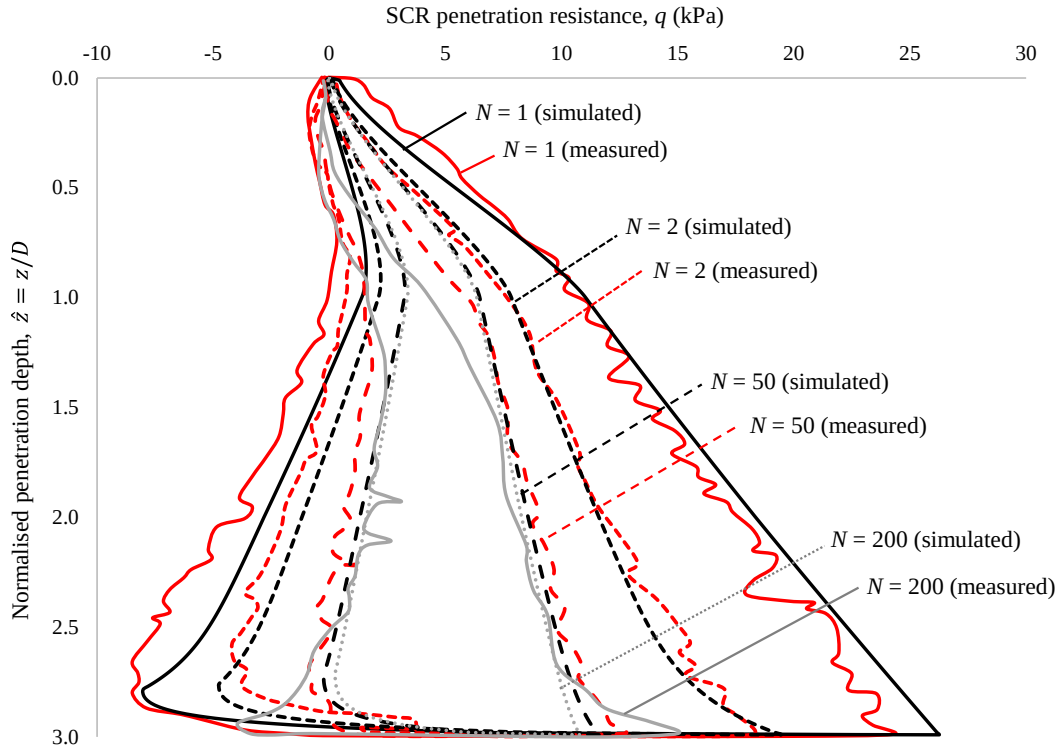

(b)

Figure 7 Comparison of experimental and predicted SCR penetration resistance during short-term test: (a) normalised seabed resistance, $q_{s,N}/q_{s,1}$, at a depth of $\hat{z}$ = 2; (b) SCR penetration resistance profiles

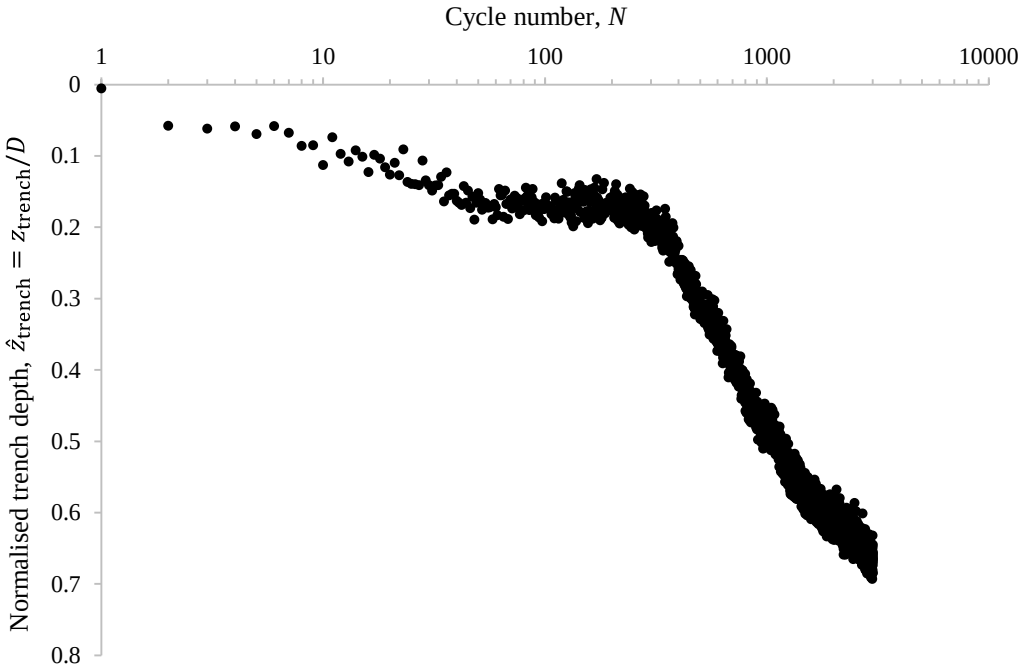

Figure 8 Development of trench during long term test (after Yuan *et al.* 2017)

841

842

843

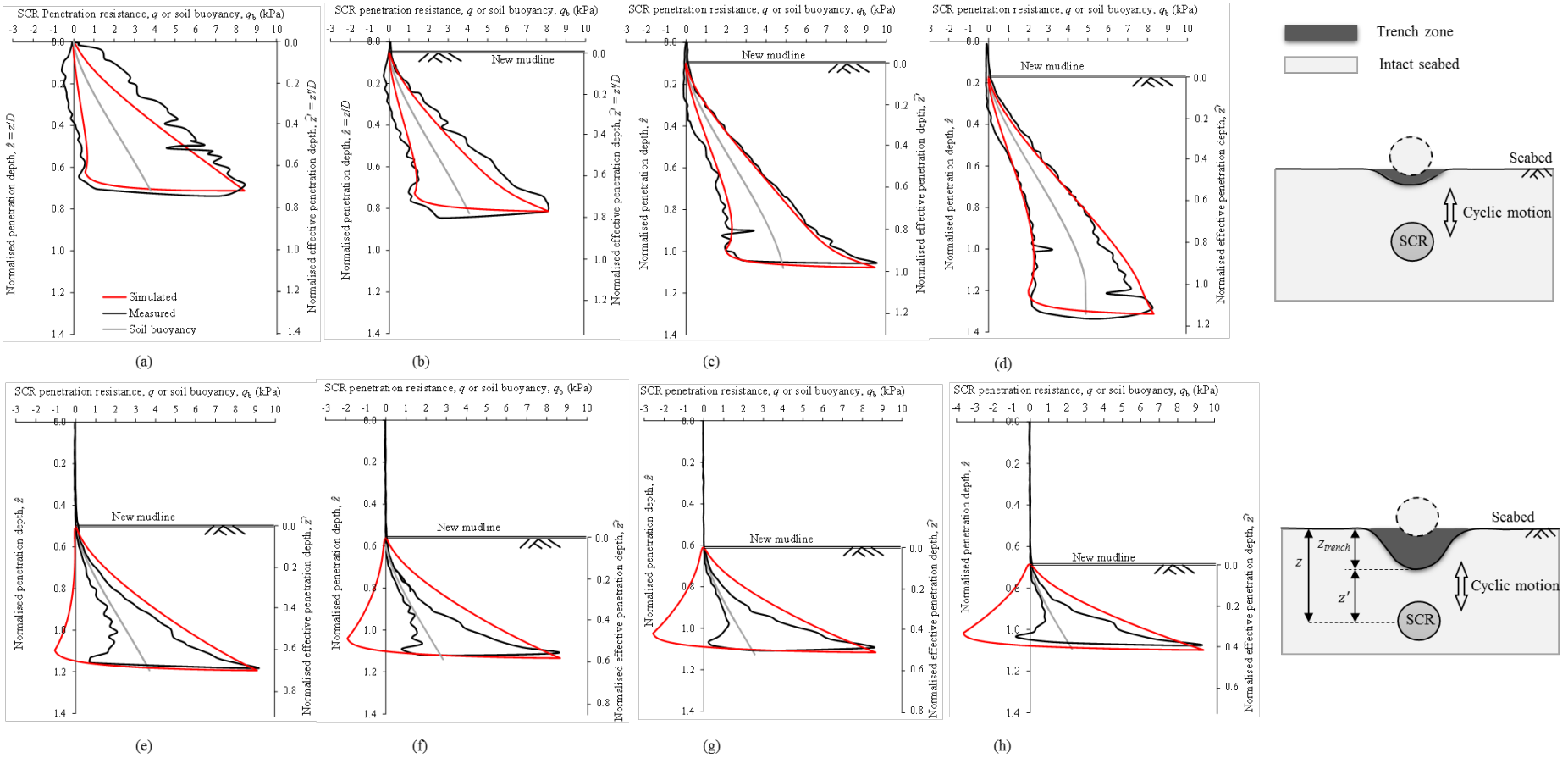

Figure 9 Comparison of experimental and predicted responses during long term test: (a) N = 1; (b) N = 2; (c) N = 10; (d) N = 100; (e) N = 1,000; (f) N = 1,500; (g) N = 2,000; (h) N = 3,000

844

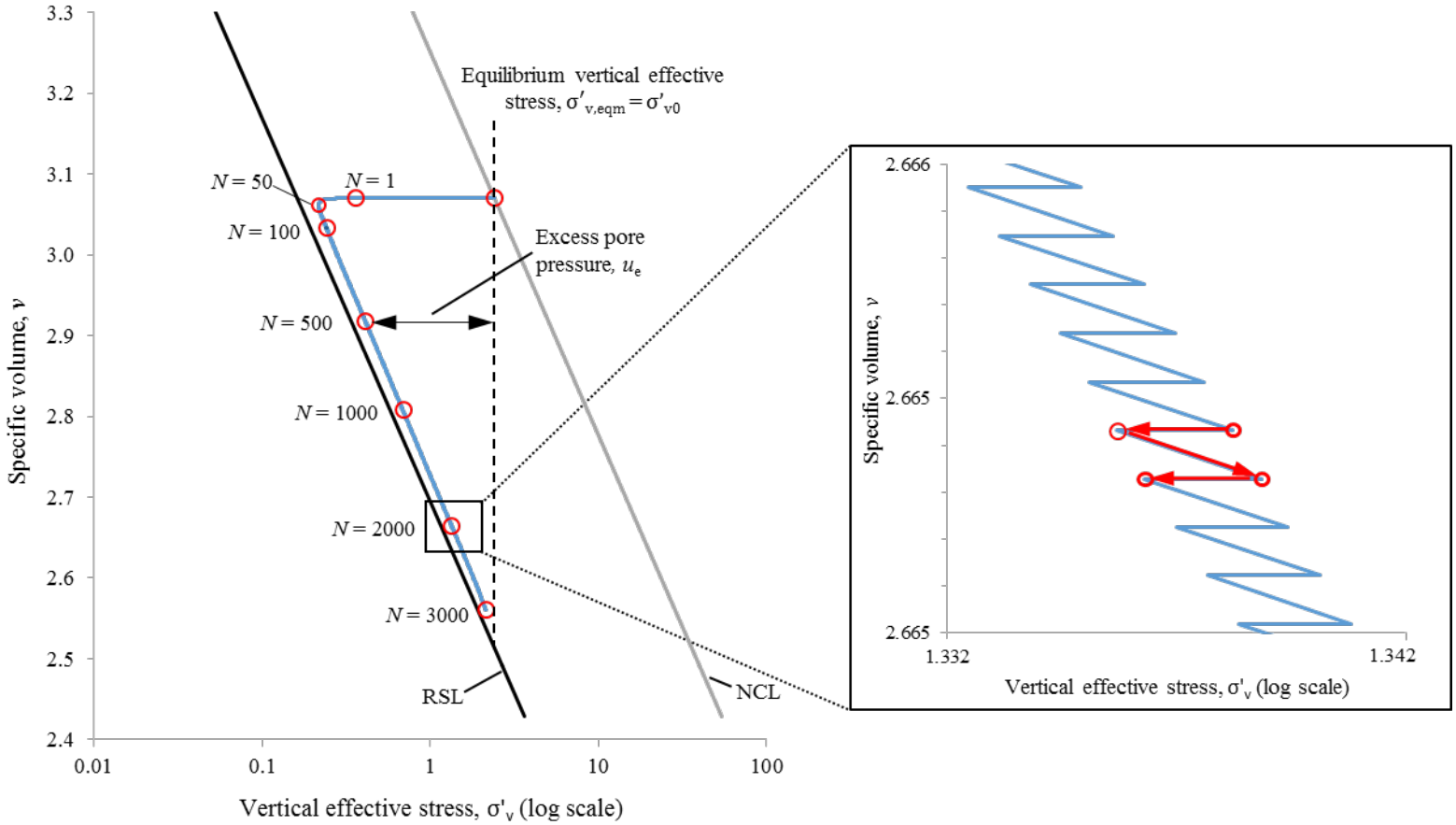
Equilibrium vertical effective stress, σ'v,eqm = σ'v0
N = 1
N = 50
N = 100
N = 500
N = 1000
N = 2000
N = 3000
Excess pore pressure, ue
RSL
NCL
Specific volume, v
Vertical effective stress, σ'v (log scale)
3.3
3.2
3.1
3.0
2.9
2.8
2.7
2.6
2.5
2.4
0.01
0.1
1
10
100
2.666
2.665
2.665
1.332
1.342

(a)

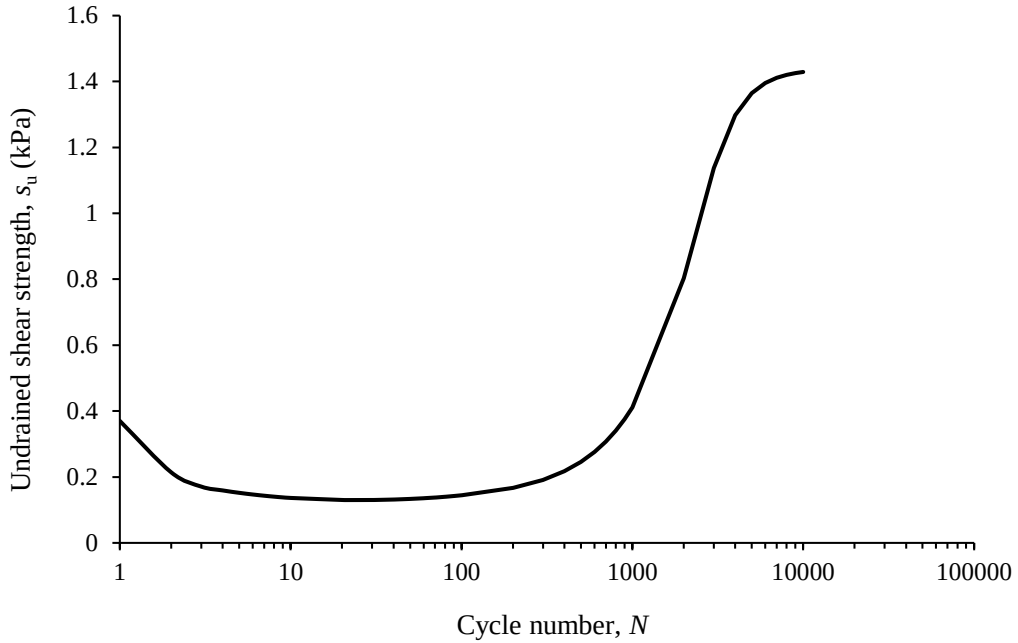

(b)

Figure 10 Calculated soil response at $\widehat{\boldsymbol{z}'}$ = 0.4 in the long-term test: (a) Variation in effective stress state; (b) changing undrained shear strength

845

846

847

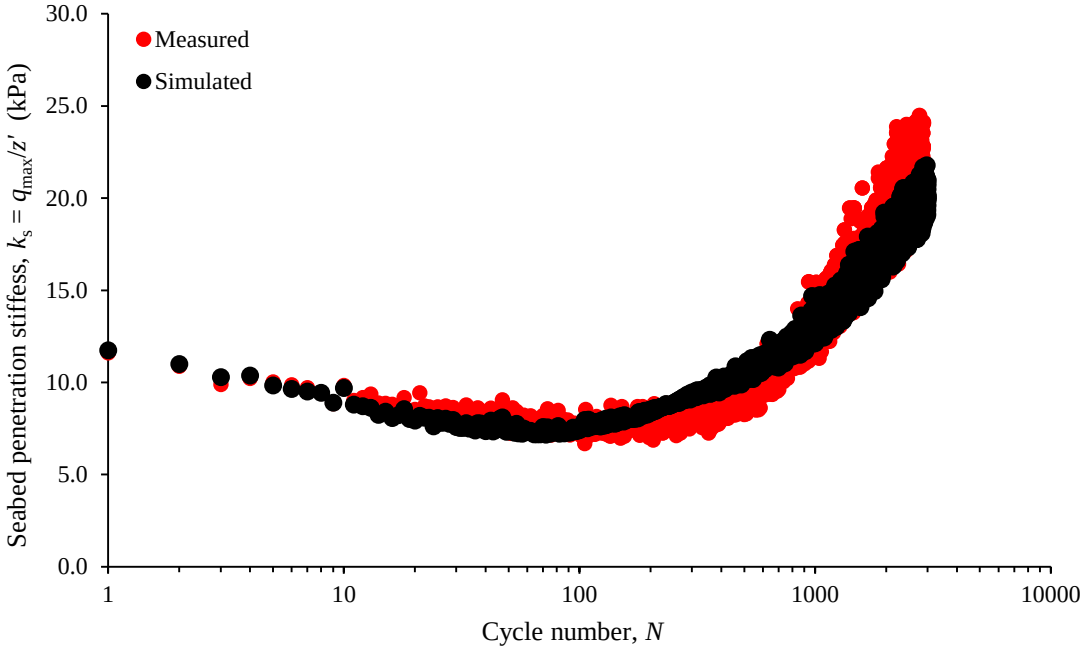

Figure 11 Comparison of experimental and predicted seabed penetration stiffness during long-term cyclic penetration

848

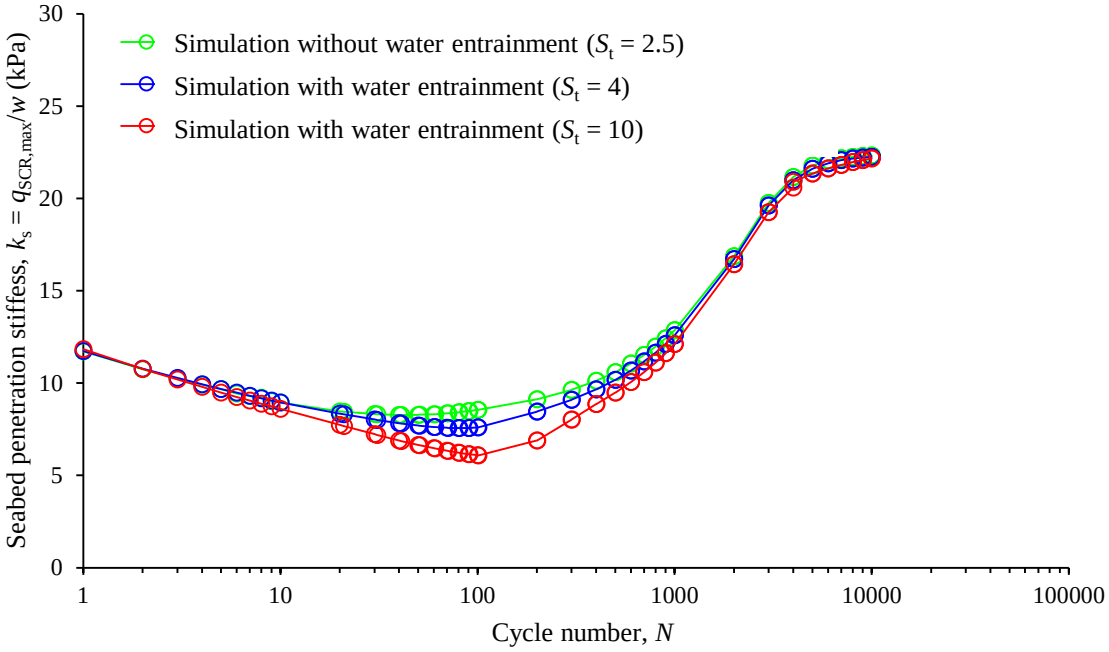

Figure 12 Effect of water entrainment on seabed penetration stiffness (penetration with a constant applied pressure q_p = 8 kPa for each cycle)

849

850

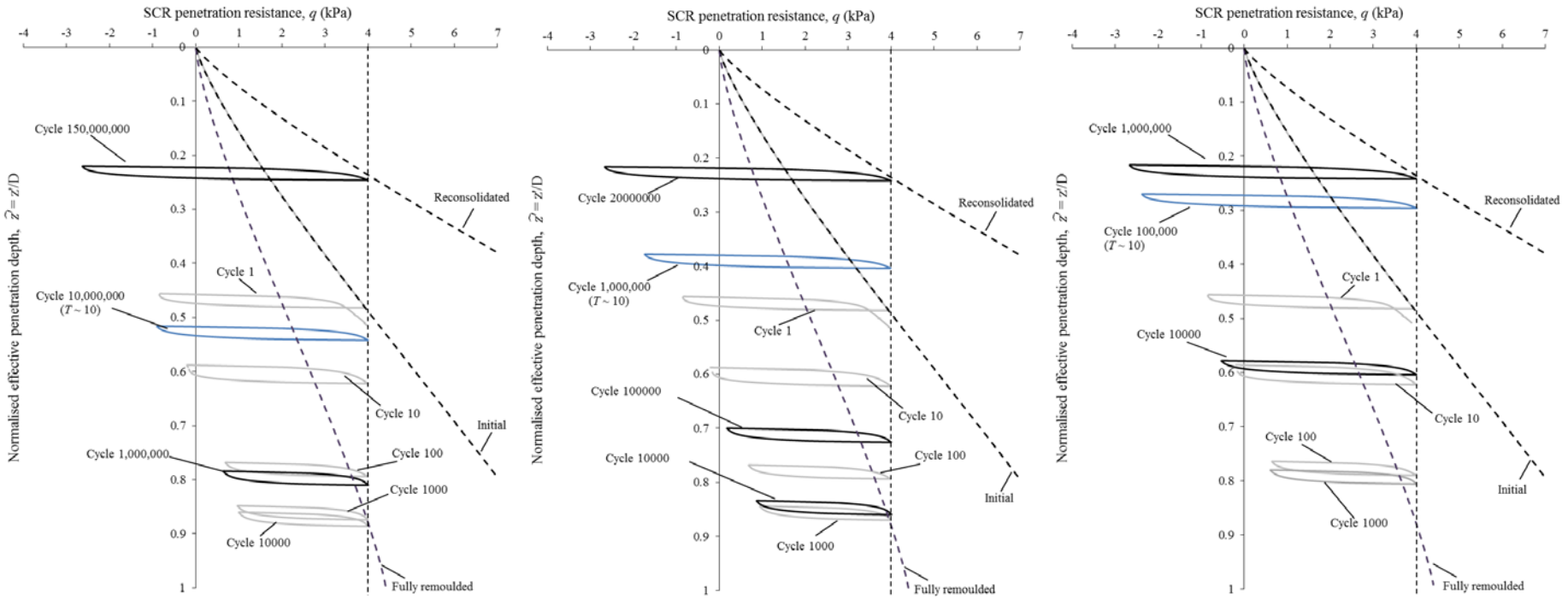

(a) (b) (c)

Figure 13 Example simulation of the whole-life change in SCR penetration resistance over long-term cycles: (a) case 2: c_v = 1 m^2/year; (b) case 6: c_v = 10 m^2/year; (c) case 10: c_v = 100 m^2/year. (All three cases with penetration to q = 4 kPa followed by an extraction displacement of 0.025D)

851

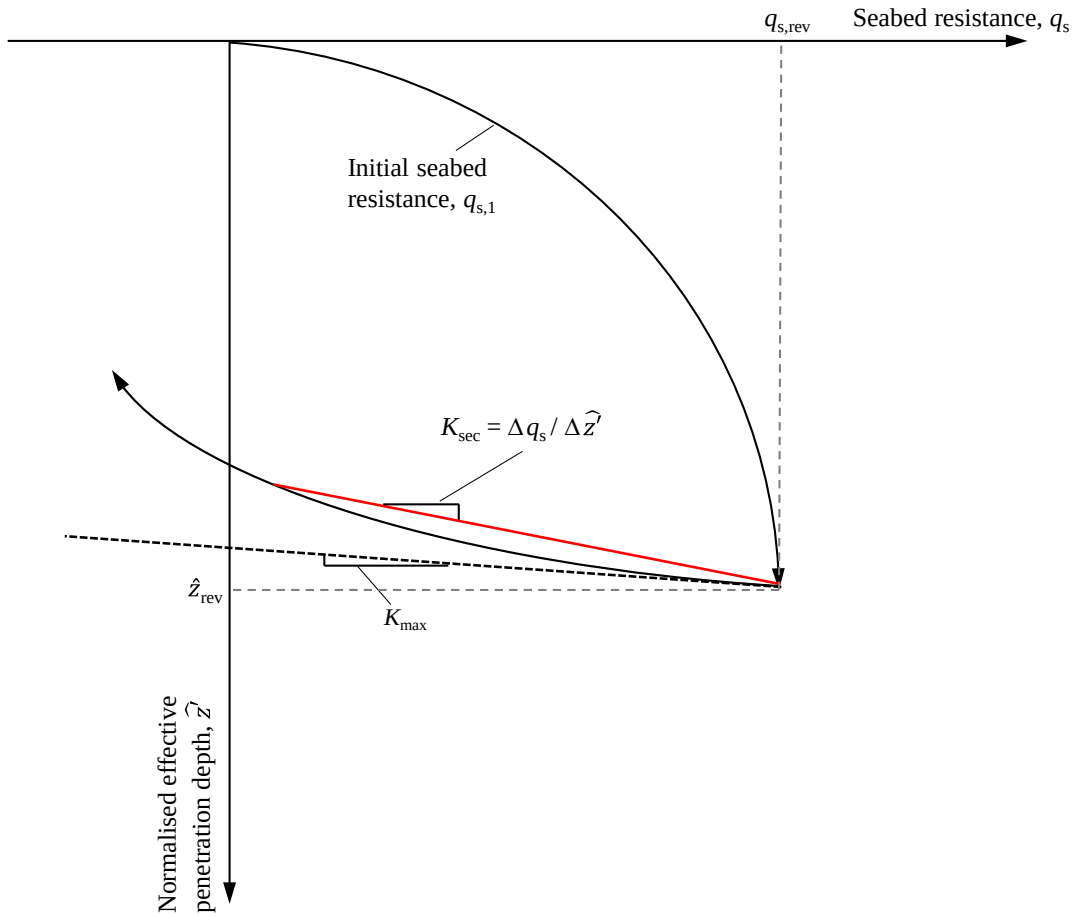

Figure 14 Definition of unloading secant stiffness, K_{sec}

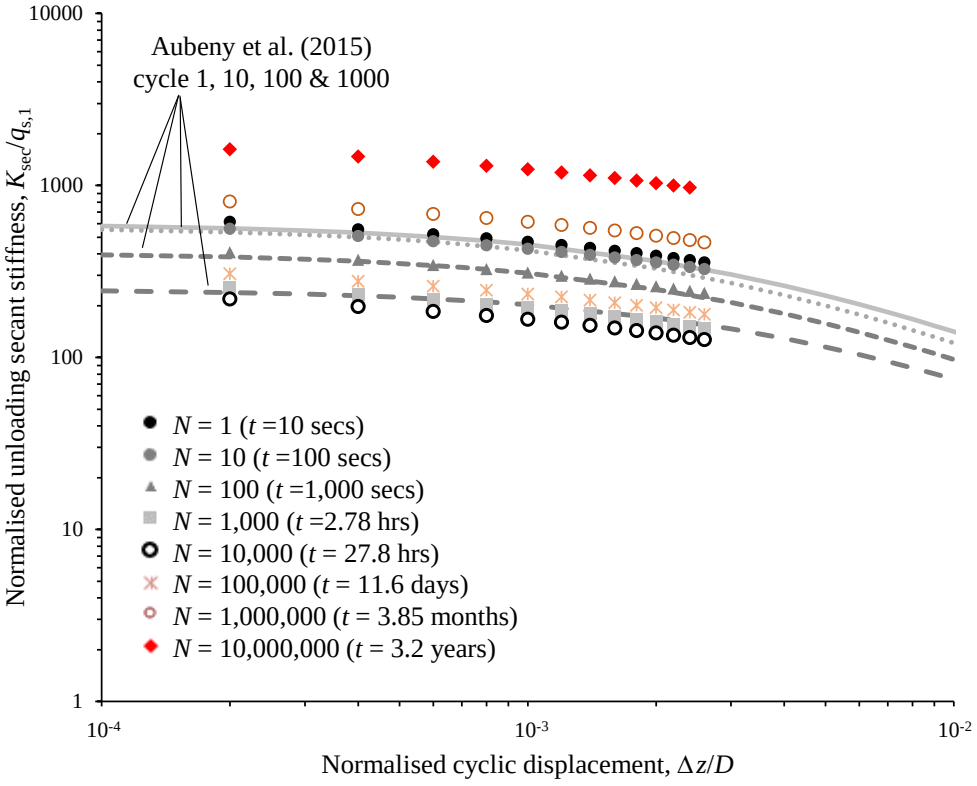

(a)

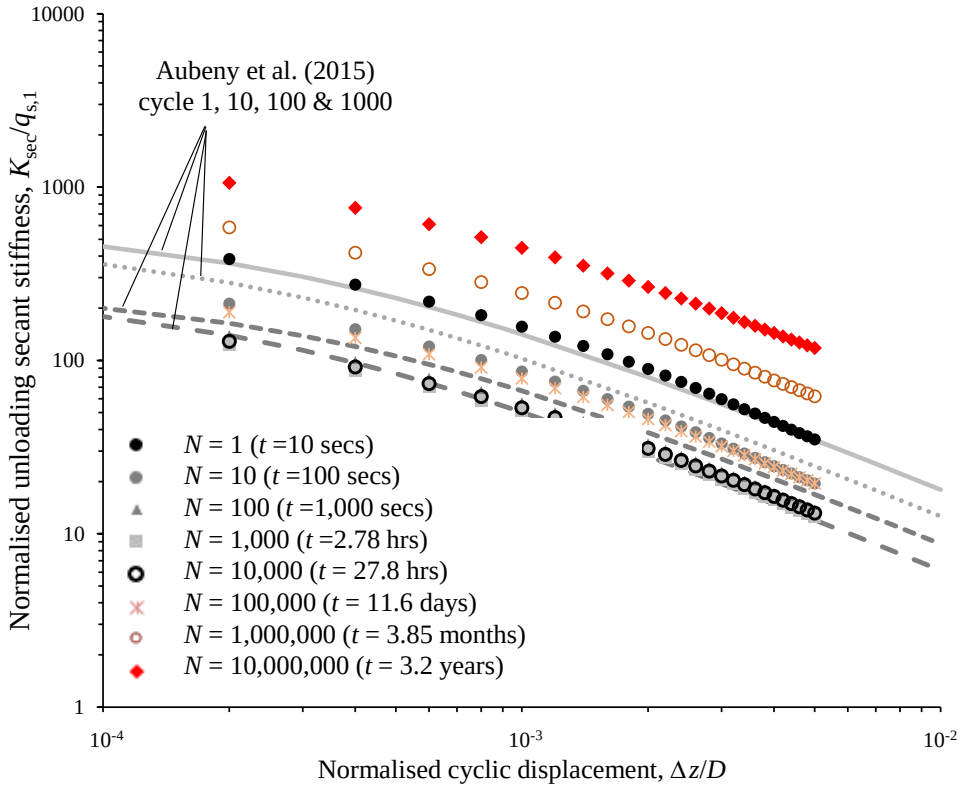

(b)

Figure 15 Variation in unloading secant stiffness: (a) case 5; (b) case 7;

863

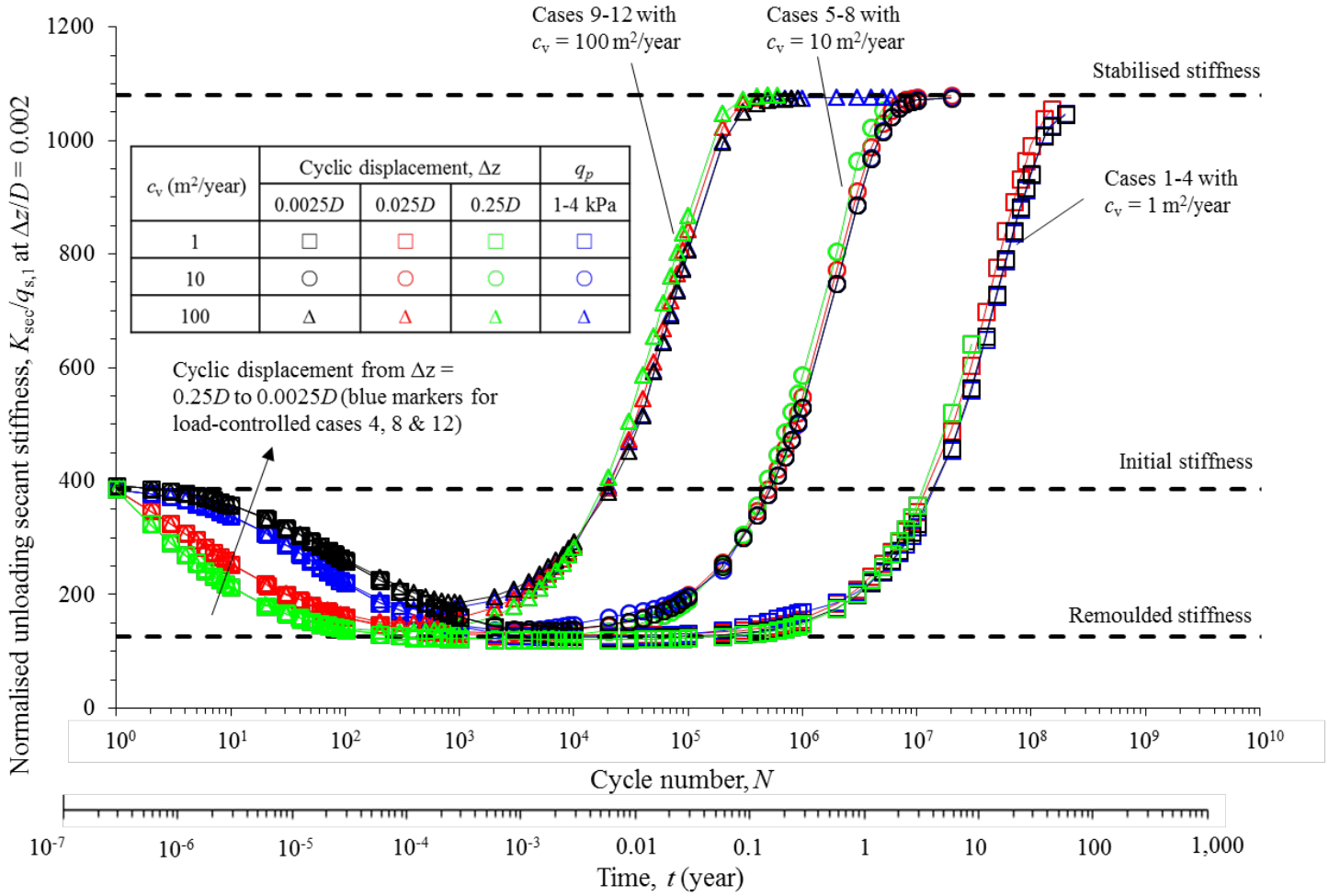
Cases 9-12 with
c_v = 100 m²/year
Cases 5-8 with
c_v = 10 m²/year
Stabilised stiffness
Cases 1-4 with
c_v = 1 m²/year
Initial stiffness
Remoulded stiffness
Cyclic displacement from Δz = 0.25D to 0.0025D (blue markers for load-controlled cases 4, 8 & 12)
c_v (m²/year)
Cyclic displacement, Δz
q_p
0.0025D
0.025D
0.25D
1-4 kPa
1
10
100
Normalised unloading secant stiffness, $K_{sec}/q_{s,1}$ at Δz/D = 0.002
Cycle number, N
Time, t (year)

(a)

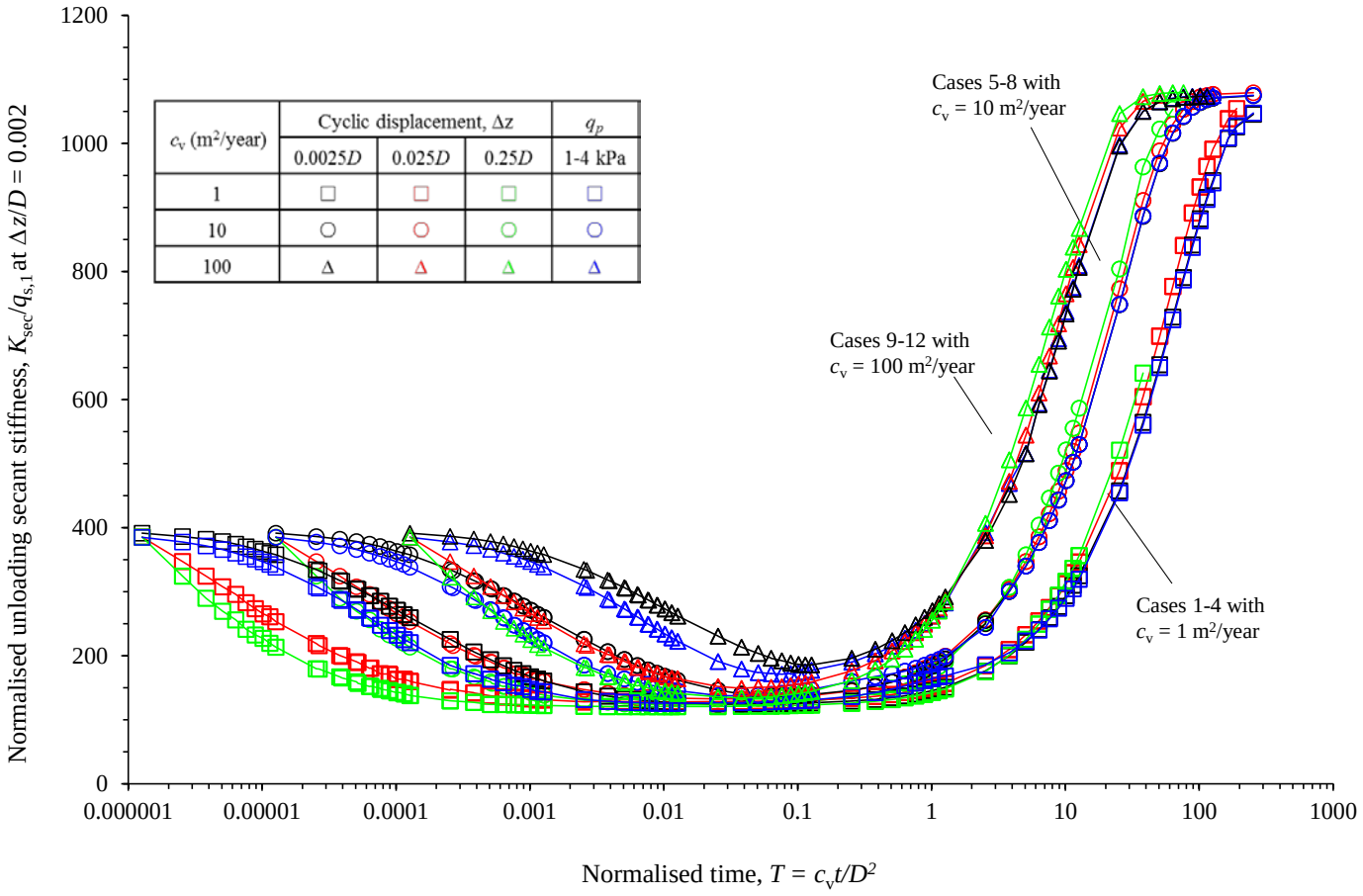

(b)

Figure 16 Evolution of normalised unloading secant stiffness, $K_{sec}/q_{s,1}$, at $\Delta z/D = 0.002$: (a) shown against cycle number, N, and time, t; (b) shown against normalised time, T

864

865

866 Table 1 SCR-seabed interaction models

SCR-seabed interaction analysis	Seabed hysteretic load-displacement modes		Effect of water entrainment	Stress domain	Cyclic loading effect		Consolidation effect	
	Open' loop	Closed' loop			Strength/ resistance	Stiffness	Strength/ resistance	Stiffness
Bridge *et al.*, 2004	No	Yes	No	Total stress	Scaled by a simple constant factor		Scaled by a simple constant factor	
You *et al*.2008	Yes	No			Scaled by simple constant factors		No	
Aubeny & Biscontin, 2009	No	Yes			No			
Randolph & Quiggin, 2009	Yes	No			Scaled by an exponential equation			
Voie *et al*. 2014	No	Yes			No			
Zargar 2017	Yes	No			Accounts for degradation with cycle number			
Clukey & Zakeri 2017	No	No			Assumes fully remoulded conditions			
This study	Yes		Yes	Effective stress	Full range of soil strength and stiffness degradation with cyclic loading		Includes effect of full or partial consolidation on seabed strength and stiffness	

867

868

869 Table 2 Summary of framework parameters

Framework component	Parameter	Description	Value
Geometry	D	Diameter of SCR (prototype scale)	1 m
Soil characteristics	γ'	Effective unit weight	6 kN/m^3
	OCR	Over-consolidation ratio	1
	$S_{t,cyc}$	Sensitivity	2.5 (4)*
Critical state mode	λ	Compression index	0.205
	κ	Swelling index	0.044
	Λ	Plastic volumetric strain ratio	0.6
	$(s_u/\sigma'_{vo})_{NC}$	Normally consolidated undrained strength ratio	0.16
	Γ_{NCL}	Specific volume, v, at σ'_v=1 kPa on NCL	3.251
Excess pore pressure generation	ε_{99}	Cumulative shear strain parameter	100 (600)*
	p	Shear strain rate parameter	2.6 (2.95)*
	β	Strain influence zone extent	0.5D
Consolidation process	T_{50}	Non-dimensional time for 50% consolidation	0.09
	m	Embedment level parameter	1.4
General soil strength and stiffness response	Φ_{steady}	Strength parameter at steady, remoulded conditions	0.6
	α	Strength influence zone extent	0.5D
	K_{max}	Maximum tangent stiffness	200
	ζ	Power law parameter for strength mobilisation	0.32

870 * values in brackets consider water entrainment

871

872

873

874

875

876 Table 3 Summary of framework parameters for simulation cases

Framework component	Parameter	Description	Value	Notes on selection or source of selected value
Geometry	D	Diameter of SCR (prototype scale)	0.5 m	Typical SCR diameter
Soil characteristics	γ'	Effective unit weight	5.5 kN/m^3	Young et al. (2000)
	OCR	Over-consolidation ratio	1	
	$S_{t,cyc}$	Sensitivity	3.5	
Critical state mode	λ	Compression index	0.205	λ from the CRSC tests for clay in GOM (Long et al. 2011)
	κ	Swelling index	0.034	κ is obtained assuming $\lambda/\kappa = 6$
	$(s_u/\sigma'_{vo})_{NC}$	Normally consolidated undrained strength ratio	0.36	Based on an undrained shear strength gradient with depth of 2 kPa/m and $\gamma' = 5.5$ kN/m^3
	Γ_{NCL}	Specific volume, v, at $\sigma'_v = 1$ kPa on NCL	1.9	Long et al. (2011)
Excess pore pressure generation	ε_{99}	Cumulative shear strain parameter	100	ε_{99} and p for excess pore pressure generation determined by giving an initial strength gradient of k = 2 kPa/m
	p	Shear strain rate parameter	2.3	
	β	Strain influence zone extent	0.5D	See section 3.1
Consolidation process	T_{50}	Non-dimensional time for 50% consolidation	0.09	See section 3.1
	m	Embedment level parameter	1.4	
General soil strength and stiffness response	Φ_{steady}	Strength parameter at steady, remoulded conditions	1.08	Assume a ratio of drained to undrained soil strength = 3
	α	Strength influence zone extent	0.5D	See section 3.1
	K_{max}	Maximum tangent stiffness	400	Taken as upper bound on K_{max} = 200 – 400 in Clukey et al. (2005, 2008) and Randolph & Quiggin (2009), as the simulation adopt small displacement cycles.
	ζ	Power law parameter for strength mobilisation	0.32	See section 3.1

877
878
879
880
881

882 Table 4 Summary of simulation cases

Simulation case no.	Coefficient of consolidation, c_v (m^2/year)	Penetration	Extraction		Number of cycles, N	Duration, t (months/years)	Symbol in Figure 16
		Applied pressure, q_p (kPa)	Applied pressure, q_p (kPa)	Normalised cyclic displacement, $\Delta z/D$			
1	1	4	-	0.0025	2×10^8	60 years	□
2			-	0.025	2×10^8	60 years	□
3			-	0.25	3×10^7	10 years	□
4			1	-	1.5×10^8	45 years	□
5	10		-	0.0025	2×10^7	6.3 years	○
6			-	0.025	2×10^7	6.3 years	○
7			-	0.25	1×10^7	3.15 years	○
8			1	-	2×10^7	6.3 years	○
9	100		-	0.0025	9×10^5	3.5 months	Δ
10			-	0.025	8×10^5	3 months	Δ
11			-	0.25	6×10^5	2.3 months	Δ
12			1	-	8×10^5	3 months	Δ

883

884